Acta Pharmaceutica Sinica B 2026;16(7):4706−4724

Chinese Pharmaceutical Association
Institute of Materia Medica, Chinese Academy of Medical Sciences

Acta Pharmaceutica Sinica B

www.elsevier.com/locate/apsb
www.sciencedirect.com

ORIGINAL ARTICLE

# Bladder adaptive hydrogel scaffold with dual release, antimicrobial, immunomodulatory, and repair: DRIVER for urinary tract infections

**Zhimin Tan[a,†], Yu Liu[b,†], Xinchao Li[c,†], Qiyu He[b,†], Tao He[c], Qian Li[a,*], Changyang Gong[c,*]**

[a]*Department of Anesthesiology, West China Hospital of Sichuan University, Sichuan Province, Chengdu 610041, China*
[b]*Department of Urology, West China Hospital of Sichuan University, Sichuan Province, Chengdu 610041, China*
[c]*Department of Biotherapy, Cancer Center and State Key Laboratory of Biotherapy, West China Hospital of Sichuan University, Sichuan Province, Chengdu 610041, China*

Received 22 August 2025; received in revised form 20 November 2025; accepted 28 November 2025

**KEY WORDS**

Bladder adaptive;
Urinary tract infections;
Hydrogel scaffold;
Dual release;
Mitochondrial autophagy

**Abstract** Urinary tract infections (UTIs), especially complex or recurrent cases, present a significant challenge. Systemic antibiotics often fail to provide adequate local drug concentrations, leading to limited efficacy and relapse. Local delivery is hindered by the bladder's dynamic environment, causing rapid drug clearance. To address this, a hydrogel scaffold, DRIVER (dual release, repair of tissues, immunomodulation, vesical adaptation, elimination of pathogens, and regulation of autophagy), is designed for sustained release in sync with the infection cycle. DRIVER forms a self-regulating 3D network through dynamic bonding and metal ion coordination, ensuring stable release and adaptability. It delivers a biphasic release profile comprising an initial antimicrobial burst that rapidly suppresses acute infection, followed by a 7-day sustained release phase. *In vitro*, DRIVER retained potent antibacterial and antifungal activity against planktonic, biofilm-embedded, and intracellular pathogens, including drug-resistant strains. Notably, the hydrogel also promoted bladder and kidney repair by modulating mitochondrial activity and autophagy, pathways essential for restoring urothelial integrity. DRIVER achieved >3 log reductions in bacterial and fungal burdens, normalized urinary function, and markedly attenuated systemic and tissue inflammation. Histological analyses confirmed robust architectural recovery in both the bladder and kidney. Together, these findings establish DRIVER as a compelling therapeutic strategy for complex UTIs.

*Corresponding authors.
E-mail addresses: hxliqian@foxmail.com (Qian Li), chygong14@163.com (Changyang Gong).
[†]These authors made equal contributions to this work.
Peer review under the responsibility of Chinese Pharmaceutical Association and Institute of Materia Medica, Chinese Academy of Medical Sciences.

https://doi.org/10.1016/j.apsb.2025.12.048

## 1. Introduction

Urinary tract infections (UTIs) are among the most common urological disorders and are primarily caused by bacterial species such as *Escherichia coli*, *Klebsiella* spp., and *Enterococcus* spp., as well as fungal species like *Candida albicans*[1-3]. Current treatment strategies rely on systemic administration, which often fails due to inadequate local drug concentrations, biofilm barriers, and difficulty in clearing intracellular pathogens. This can lead to resistance and gut microbiota disruption[4-7]. Recently, the increasing prevalence of antibiotic-resistant strains and fungal infections has significantly challenged traditional antimicrobial treatments.

In contrast, catheter-based hydrogel delivery enables direct drug deposition at the infection site, minimizing systemic absorption[8]. Its biocompatibility and controlled release mechanism ensure sustained local antimicrobial activity, thereby improving therapeutic outcomes and reducing the risk of resistance[8,9]. While local delivery offers targeting advantages, several critical challenges remain. The bladder's dynamic physiology, characterized by frequent voiding, urinary flow, and mucosal turnover-causes rapid drug clearance, limiting the duration of therapeutic efficacy[10,11]. The development of intravesical hydrogel drug delivery systems still has limitations (Supporting Information Table S1). Recent advancements in multi-stage release, immune regulation, and tissue repair still struggle to integrate antimicrobial activity in the bladder's dynamic environment[12-15]. To overcome these limitations, the development of a delivery system capable of dynamic adjustment according to bladder physiology, offering multi-stage drug release, and activating immune regulation and tissue repair functions, has become a key focus of ongoing research.

UTIs treatment is particularly challenging not only due to difficulty in eradicating pathogens and frequent recurrence but also because lower urinary tract symptoms such as increased frequency, reduced voided volume and dysuria often persist after pathogen clearance. Up to 30% patients experience relapse shortly after treatment, suggesting infections may trigger lasting epithelial dysfunction[16,17]. Potential mechanisms include pathogen persistence, biofilm formation, chronic inflammation, impaired barrier repair, mitochondrial dysfunction, metabolic dysregulation, oxidative stress, and sensory nerve hypersensitization[18-20]. Of these, mitochondrial dysfunction stands out as a critical factor, as it directly impairs cellular energy production and regenerative capacity, exacerbates inflammation, and alters neuronal function, all of which contribute to the persistence and chronicity of LUTS[21,22].

Here, we introduce DRIVER, an injectable hydrogel scaffold designed specifically for the treatment of complex UTIs. DRIVER features a biphasic release system tailored to the infection cycle, delivering a rapid antimicrobial burst to control acute infection, followed by sustained drug release to extend the relief period and prevent relapse. Zinc ions and chitosan derivatives synergistically enhance the antimicrobial efficacy, further boosting DRIVER's anti-infection potential. Unlike conventional hydrogels, DRIVER forms a self-regulating 3D network through metal ion coordination and dynamic covalent bonding, improving bladder adaptability and ensuring stable drug release. This innovative design overcomes the limitations of traditional hydrogels, such as insufficient adaptability in complex urinary environments and rapid drug clearance, which often compromise therapeutic efficacy. Through its combined antimicrobial, anti-inflammatory, and reparative mechanisms, DRIVER modulates the immune microenvironment, activates mitochondrial autophagy, and promotes tissue repair, significantly enhancing treatment outcomes and reducing relapse rates. DRIVER shows substantial clinical translation potential, particularly for achieving sustained clinical remission and pathological repair in complex and recurrent UTIs.

## 2. Materials and methods

### 2.1. Materials

Sodium periodate ($NaIO_4$) was purchased from Sigma−Aldrich (USA). Sodium hyaluronate was purchased from Shanghai Bide Pharmaceutical Technology Co., Ltd. (China). Carboxymethyl chitosan was purchased from Dalian Meilun Biotechnology Co., Ltd. (China). Zinc chloride was provided by Aladdin Scientific (China). Levofloxacin and protease/phosphatase inhibitors were purchased from Abmole Bioscience Inc. (USA). Fluconazole was purchased from Dalian Meilun Biotechnology Co., Ltd. (China). Rhodamine B was purchased from Solarbio Life Sciences (China). RIPA lysis buffer was purchased from Elabscience Biotechnology Inc. (China). *E. coli* American Type Culture Collection (ATCC) 25,922 and *C. albicans* ATCC 10231 were purchased from TSTO Biological Technology Co., Ltd. (China). *E. coli* Culture Collection University of Gothenburg (CCUG) 58,541 and *Candida krusei* ATCC 6258 were purchased from BeNa Culture Collection (China). Luria Bertani (LB) broth and LB agar plates were purchased from Biosharp Life Sciences (China). Sabouraud dextrose broth and Sabouraud dextrose agar plates were purchased from Qingdao Hopebio Technology Co., Ltd. (China). Yeast Malt (YM) agar plates and Columbia blood agar plates were purchased from BeNa Culture Collection (China). SV-Human urethral epithelial cells (SV-HUC) and RAW264.7 macrophages were obtained from Hysigen (China). Ham's F-12K medium was purchased from Hysigen (China), and high-glucose Dulbecco's modified Eagle's medium (DMEM) was purchased from Gibco (USA). Fetal bovine serum (FBS) and penicillin−streptomycin (1%) were purchased from Gibco (USA). ELISA kits for IL-6, TNF-$\alpha$, and CRP were purchased from Wuhan Fine Biotech Co., Ltd. (China). Anti-phospho-ULK1 antibody was purchased from Cell Signaling Technology (USA). Anti-ULK1, anti-LC3, anti-P62, and anti-GAPDH antibodies were purchased from Proteintech (USA). Anti-ATG5 antibody was purchased from ABclonal (China). Anti-TOMM20 and anti-TOMM70 antibodies, as well as anti-PINK1 and anti-Parkin antibodies, were purchased from Affinity Biosciences (USA). Corresponding fluorescent secondary antibodies were purchased from Cell Signaling Technology (USA).

### 2.2. Cells, strains, and animals

SV-HUC cells and RAW264.7 macrophages were cultured in F-12K medium and high-glucose DMEM, respectively, both

supplemented with 10% FBS and 1% penicillin−streptomycin. *E. coli* ATCC 25922 and *C. albicans* ATCC 10231 were used as reference strains to evaluate drug efficacy under sensitive conditions, while *E. coli* CCUG 58541 (multidrug resistant) and *C. krusei* ATCC 6258 (fluconazole resistant) were included to assess efficacy in resistant backgrounds. *E. coli* ATCC 25922 (LB agar, 37 °C, 24 h), *C. albicans* ATCC 10231 (Sabouraud dextrose agar, 30 °C, 48 h), *E. coli* CCUG 58541 (Columbia blood agar, 37 °C, 24 h), and *C. krusei* ATCC 6258 (YM agar, 30 °C, 48 h) were cultured under their respective conditions. For liquid cultures, *E. coli* strains were grown in LB broth (37 °C, 24 h), while *C. albicans* and *C. krusei* in Sabouraud dextrose broth (30 °C, 48 h). Female C57BL/6 mice (6−8 weeks old) were purchased from GemPharmatech (Nanjing, China). All animals were housed under specific-pathogen-free conditions on a 12-h light/12-h dark cycle, and all procedures were approved by the Animal Ethics Committee of Sichuan University and performed in accordance with institutional guidelines. All animal experiments complied with national animal welfare regulations and were approved by the Experimental Animal Ethics Committee of West China Hospital, Sichuan University, China (No. 20250516001).

### 2.3. Preparation and purification of oxidized hyaluronic acid (OHA)

Sodium hyaluronate was dissolved in deionized water to prepare an aqueous hyaluronic acid (HA) solution. $NaIO_4$ was then added, and the mixture was stirred vigorously at 37 °C for 12 h in the dark. Subsequently, ethylene glycol was added to quench excess $NaIO_4$, and stirring continued for additional 2 h. The raw compounds were then dialyzed within deionized water for 3 days to remove residual reagents. The final OHA product was stored in a vacuum desiccator for further use.

### 2.4. Hydrogel preparation and characterization

*N*,*O*-Carboxymethyl chitosan (NOCC) was obtained from Dalian Meilun Biotechnology (China) and dissolved in sterile deionized water at 20 mg/mL. To optimize the formulation, OHA solutions with various oxidation degrees (20%, 30%, 40%, and 50%) were mixed with NOCC at different ratios (*e.g.*, OHA: NOCC = 10:90, 20:80, 30:70), and $ZnCl_2$ was added at final concentrations of 10−30 mg/mL. Gelation was evaluated at 37 °C to identify formulations that formed stable gels within 10 min without precipitation or fluid retention, ensuring good injectability and *in situ* gelation properties. The optimal formulation consisted of OHA (40% oxidation, 20 mg/mL), NOCC (20 mg/mL), and $ZnCl_2$ (10 mg/mL) in a 20:80:2 ratio. Upon mixing, Schiff base reactions followed by $Zn^{2+}$-induced coordination interactions occurred sequentially, forming a dynamically co-crosslinked hydrogel used for subsequent performance evaluations and drug loading experiments. For drug loading, levofloxacin or fluconazole was dissolved in the OHA solution, followed by the addition of $ZnCl_2$ and NOCC to complete the gelation and drug encapsulation. In preliminary optimization studies, release supernatants collected from drug-loaded hydrogels with graded drug-to-hydrogel ratios (200, 400, 800, 1600, and 3200 μg/mL; corresponding to 10, 20, 40, 80, and 160 μg per 50 μL hydrogel) were systematically evaluated for their antimicrobial potency against *E. coli* ATCC 25922, *E. coli* CCUG 58541, *C. albicans* ATCC 10231, and *C. krusei* ATCC 6258 (Section 3.3.). Hydrogels within the higher loading range exhibited markedly enhanced bactericidal and fungicidal activities, particularly in disrupting biofilm architecture. Based on this screening, loading doses of 100 μg levofloxacin or 150 μg fluconazole per 50 μL hydrogel were selected for subsequent animal experiments, as these concentrations achieved potent antibacterial and antifungal effects while satisfying the requirements for appropriate gelation kinetics and mechanical stability.

The chemical modification of OHA was confirmed by $^1$H nuclear magnetic resonance ($^1$H NMR) based on characteristic shifts indicating aldehyde group formation. Fourier-transform infrared (FTIR) was performed over the range of 400−4000 $cm^{-1}$ to analyze HA, OHA, and NOCC, with particular attention to the appearance or changes of functional group peaks (*e.g.*, C═O, −OH, $-NH_2$) associated with oxidation and covalent interactions. The microstructure of the hydrogels was examined using scanning electron microscopy (SEM). Samples were freeze-dried and sputter-coated with gold to improve conductivity and imaging resolution. SEM images were used to evaluate the three-dimensional porous architecture and uniformity of pore distribution, with porosity quantified *via* ImageJ-based image analysis. Rheological properties were assessed using a rotational rheometer (TA Instruments Discovery HR-20) at 37 °C. Storage modulus ($G'$) and loss modulus ($G''$) were recorded over time under a constant shear frequency of 1 Hz and strain of 0.5% to simulate the *in situ* sol−gel transition and evaluate both injectability and post-gelation mechanical stability.

### 2.5. In vitro swelling and weight retention tests

Swelling ratio test: Freshly prepared hydrogel samples were weighed to determine the initial wet weight ($W_i$) and then incubated in 37 °C PBS. At 0, 6, 12, 18, and 24 h on Day 1, samples were removed, surface moisture was gently blotted with filter paper, and the wet weight ($W_s$) was recorded. The swelling ratio was calculated as Eq. (1):

$$\text{Swelling ratio}\ (\%) = (W_s / W_i) \times 100 \quad (1)$$

Weight retention test: Fresh hydrogel samples were freeze-dried, and the initial dry weight ($W_{d0}$) was recorded. Fresh samples were incubated in 37 °C PBS, and at 24-h intervals, samples were removed, surface moisture blotted, and then freeze-dried again to record the dry weight ($W_d$) after incubation. The weight retention was calculated as Eq. (2):

$$\text{Weight retention}\ (\%) = (W_d / W_{d0}) \times 100 \quad (2)$$

Every 24 h, 1 mL of PBS was removed and replaced with an equal volume of fresh PBS to simulate the dilution and degradation behavior of the hydrogel during continuous urine generation and voiding.

### 2.6. In vitro drug release

Standard curves for levofloxacin and fluconazole were established at $\lambda$ = 291 nm and $\lambda$ = 261 nm, respectively. Drug-loaded hydrogels (200 μL, $n$ = 5) were immersed in 1 mL of PBS and incubated under static conditions at 37 and 24 °C. At 12-h intervals, 100 μL of supernatant was collected from each well and analyzed using Ultraviolet−Visible (UV−Vis) spectrophotometer. After measurement, the sampled volume was returned to maintain system volume and drug mass balance. To mimic urinary turnover, 1 mL of PBS was replaced with fresh PBS every 24 h to simulate dynamic dilution and diffusion in the bladder environment. To

simulate the human urinary environment, fresh, clean midstream urine was collected from healthy adult volunteers. Drug-loaded hydrogels (200 μL, $n = 3$) were immersed in 1 mL of urine and incubated statically at 37 °C. All urine samples were anonymously obtained, centrifuged (3000 rpm, 10 min), and filtered (0.22 μm) prior to use to remove debris and microorganisms, ensuring sterility and consistency. Drug concentrations over time were measured using ultra performance liquid chromatography tandem mass spectrometry (UPLC−MS/MS).

### 2.7. Drug concentration analysis

Urine samples were collected on Days 1, 3, 5, and 7 after intravesical administration of the drug-loaded hydrogel. The absorbance of levofloxacin and fluconazole was measured at $\lambda = 291$ nm and $\lambda = 261$ nm, respectively, using a UV−Vis spectrophotometer. To eliminate interference from endogenous urinary components, the absorbance values of corresponding blank urine samples were subtracted from those of the drug-containing samples. The corrected absorbance values were then used to calculate the actual drug concentrations based on standard calibration curves.

Due to matrix interference and the limited sensitivity of UV−Vis in urine, UPLC−MS/MS was additionally used for precise quantification of drug concentration in the samples. A 0.1 mL aliquot of serum or urine was mixed with 0.3 mL methanol, vortexed for 1 min, and ultrasonicated at 4 °C for 30 min. The mixture was centrifuged at 10,000 rpm for 10 min, and the supernatant was evaporated under nitrogen. The residue was reconstituted in 0.1 mL initial mobile phase, vortexed, centrifuged, and filtered through a 0.22 μm membrane before analysis. For bladder tissue, 0.02 g was homogenized in 0.2 mL ice-cold saline, then ultrasonicated for 30 min. After adding 0.6 mL methanol, the sample was centrifuged at 10,000 rpm for 10 min. The supernatant was evaporated under nitrogen, reconstituted in 0.1 mL initial mobile phase, vortexed, centrifuged, and filtered. Standards (fluconazole and levofloxacin, purity ≥98%) were stored at −20 °C and used to prepare working solutions. Chromatographic analysis was performed using a UPLC system (Waters, USA) with a YMC-Triart C18 column (2.1 mm × 100 mm, 1.7 μm). The mobile phase consisted of 0.1% formic acid in water (A) and acetonitrile (B), at 0.3 mL/min flow rate, 35 °C column temperature, and 10 μL injection volume. Mass spectrometry was conducted on a 4000 QTRAP (AB Sciex, USA) in positive electrospray ionization mode ($ESI^+$) with ion source temperature 450 °C, spray voltage +5500 V, curtain gas 35 psi, collision gas 7 psi, and source gases 40/50 psi.

### 2.8. Inductively coupled plasma-mass spectrometry (ICP-MS)

Zinc content in serum, urine, and bladder samples was measured using an inductively coupled plasma mass spectrometer (ICP-MS, PerkinElmer NexION 300D, USA). Serum and urine (0.02 mL) were mixed with 2% ultrapure nitric acid and diluted to 10 mL in clean 15 mL centrifuge tubes, filtered through a 0.22 μm membrane, and analyzed after appropriate dilution. Bladder tissue (0.010−0.070 g) was digested in polytetrafluoroethylene microwave vessels with 10 mL ultrapure nitric acid, followed by predigestion at 120 °C for 20 min. After cooling, 5 mL nitric acid was added, sealed, and digestion continued in a microwave system (Touchwin 2.0, China). After digestion, samples were acid-digested at 180 °C for 30 min until 1 mL of clear solution remained. The samples were diluted to 50 mL with ultrapure water, filtered, and analyzed. ICP-MS conditions were: RF power 1200 W, cooling gas 15 L/min, carrier gas 1.0 L/min, sampling depth 6 mm, and isotopes $^{66}Zn$ and $^{68}Zn$ monitored. Quantitative analysis was performed using external calibration, with daily instrument calibration using multi-element standards.

### 2.9. Hydrogel bladder retention experiment

6−8-week-old female C57BL/6 mice (18−22 g) were fasted and deprived of water for 12 h prior to the experiment. Anesthesia was induced using 2%−3% isoflurane *via* inhalation, and the mice were positioned supine after confirming the absence of pain responses. A lubricated polyethylene catheter (PE-10, outer diameter 0.61 mm) was connected to a syringe and slowly inserted into the bladder *via* the urethra (approximately 2 cm depth). Based on preliminary experiments, the total injection volume was adjusted to ensure 50 μL of liquid hydrogel was injected into the bladder. After injection, the mice were kept in the supine position for 15 min to allow *in situ* gelation of the hydrogel. Mice were euthanized on days 1, 3, 5, and 7 post-injection, and the bladder was exposed *via* abdominal incision. Hydrogel residue, its attachment location, and morphological changes were observed. All procedures were conducted under sterile conditions.

### 2.10. In vivo fluorescence imaging

Rhodamine B was added to the OHA solution at a final concentration of 0.01% (*w/v*, relative to the injection volume) to prepare the fluorescently labeled hydrogel precursor. After sequential mixing with NOCC and $ZnCl_2$, the formulation was administered into the bladder of female C57BL/6 mice (injection volume: 50 μL) *via* a lubricated polyethylene catheter. Fluorescence signals in the bladder region were recorded using the IVIS spectrum imaging system on Days 0, 1, 3, 5, 7, and 9 post-injection to assess *in vivo* localization stability and retention. Mice were maintained under continuous isoflurane anesthesia during imaging, and background fluorescence was subtracted using a blank control group.

### 2.11. Minimum inhibitory concentration (MIC) determination and growth curve analysis

The MIC of drug-loaded hydrogels was determined using the microdilution method in a 96-well plate. Hydrogels containing different concentrations of levofloxacin or fluconazole were incubated with bacterial suspensions of *E. coli* ATCC 25922 and CCUG 58541 [$1 \times 10^7$ colony-forming units (CFU)/mL, 24 h] or *C. albicans* ATCC 10231 and *C. krusei* ATCC 6258 ($1 \times 10^6$ CFU/mL, 48 h). After incubation, the optical density at 600 nm (optical density $OD_{600}$) was measured to determine the MIC range. Drug-loaded hydrogel and free drug groups were incubated with *E. coli* ATCC 25922 or *C. albicans* ATCC 10231 suspensions at concentrations determined from the MIC range for 48 h. $OD_{600}$ was measured at 0, 2, 4, 6, 8, 12, 24, 36, and 48 h, and growth curves were constructed to evaluate the antimicrobial effect.

### 2.12. Minimal biofilm inhibitory concentration (MBIC) and minimal biofilm eradication concentration (MBEC)

Bacterial and fungal biofilm assays were performed with standard methods, optimized as needed[23]. A 1 mL suspension of bacteria ($1 \times 10^7$ CFU/mL) or fungi ($1 \times 10^6$ CFU/mL) was added to a 24-

well plate and incubated at 37 °C for 48 h to form mature biofilms. After incubation, the supernatant was discarded, and biofilms were washed three times with PBS. Biofilm biomass was measured by crystal violet staining: 30 min of staining, followed by three PBS washes and air drying. Dye was dissolved with 95% ethanol for 5 min, and absorbance at $OD_{600}$ was recorded. Biofilm disruption was calculated as Eq. (3):

$$\text{Disruption rate}\ (\%) = \left(OD_{control} - OD_{experimental}\right) / OD_{control} \times 100 \quad (3)$$

The MBIC assessed biofilm formation inhibition, with bacterial or fungal suspensions co-incubated with treatments for 48 h, followed by crystal violet staining and viable cell counting. The MBEC evaluated the removal of mature biofilms, with biofilms co-incubated with treatments for 48 h, and residual biofilm and viable cell counts determined similarly.

### 2.13. *Intracellular survival assays*

A logarithmic-phase bacterial or fungal suspension (MOI = 100) was added to each well and incubated at 37 °C, 5% $CO_2$ for 1 h. After three washes with PBS to remove free organisms, fresh sterile medium and hydrogel release solutions from different treatments were added and incubated for 23 h. At the endpoint, cells were washed, collected, and lysed with 1 mL of 1% Triton X-100 for 5 min. The lysate was centrifuged at 10,000 rpm for 5 min, and the pellet was resuspended in PBS for intracellular CFU counting.

### 2.14. *Antibacterial zone of inhibition assay*

The antibacterial activity was evaluated using the paper disc method. *E. coli* ATCC 25922 was cultured on LB agar, *E. coli*

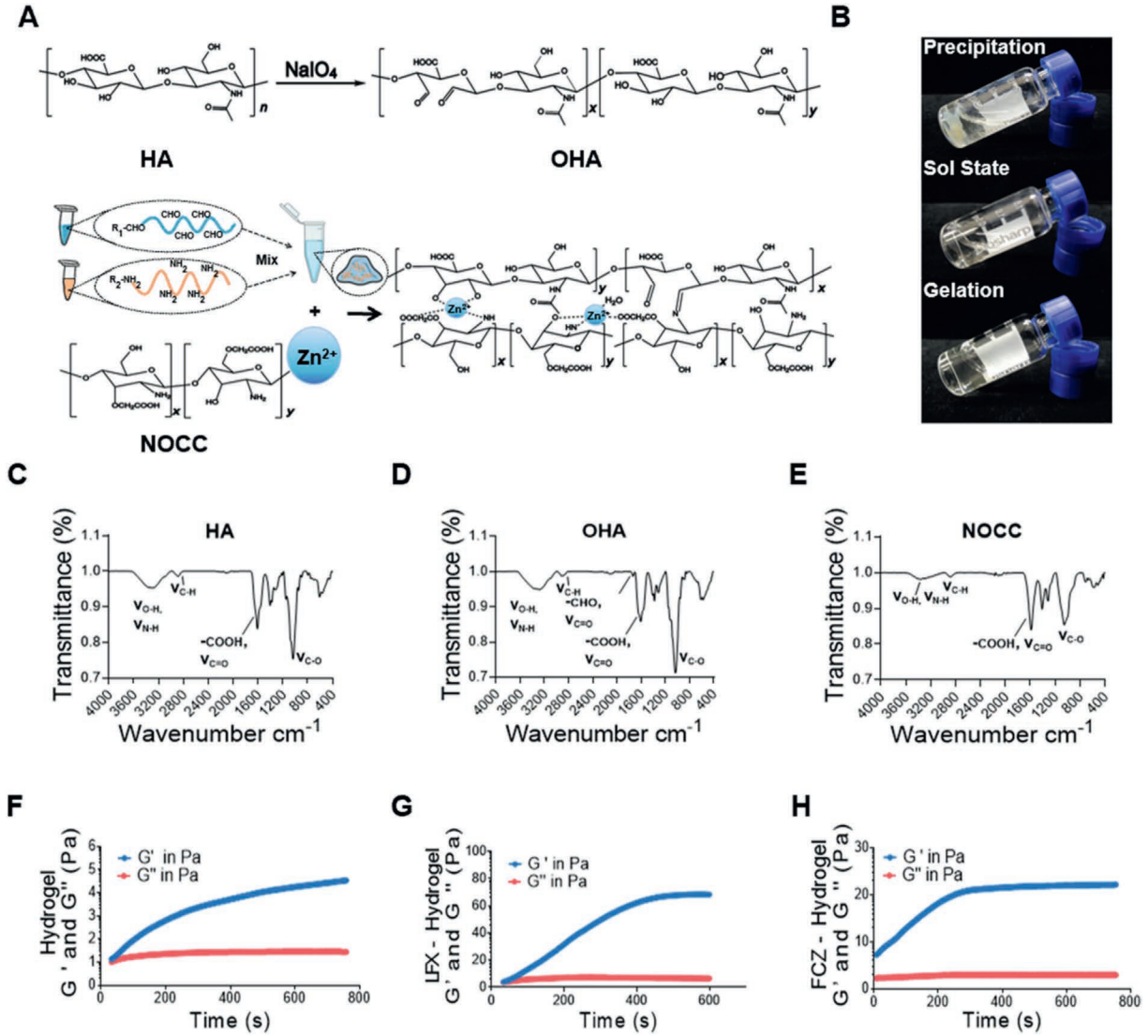


**Figure 1** Hydrogel construction and basic physicochemical characterization. (A) Schematic of the hydrogel preparation process. (B) Comparison of hydrogel appearance (Up: precipitation; Middle: sol state; Down: gelation). (C–E) FTIR spectra of HA (C), OHA (D), and NOCC (E). (F–H) Rheological curves showing storage modulus (G′) and loss modulus (G″) for blank hydrogel (F), levofloxacin-loaded hydrogel (G), and fluconazole-loaded hydrogel (H). Abbreviations: FCZ, fluconazole; FTIR, Fourier transform infrared spectroscopy; HA, hyaluronic acid; LFX, levofloxacin; $NaIO_4$, Sodium periodate; NOCC, *N*,*O*-carboxymethyl chitosan; OHA, oxidized hyaluronic acid.

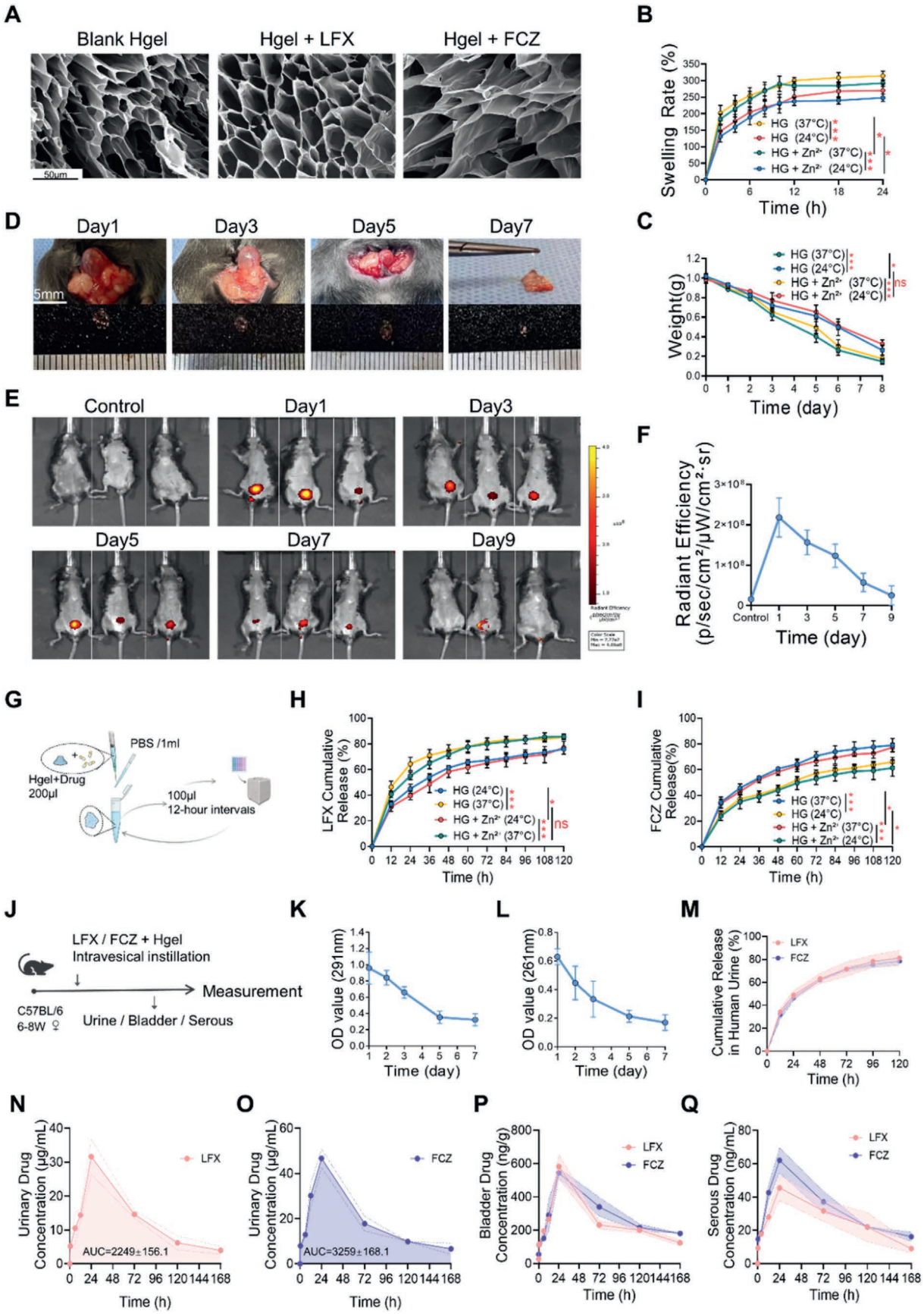


**Figure 2** Microscopic structure, physicochemical stability, and drug release performance of the hydrogel. (A) SEM images of the hydrogel's microstructure (magnification: 500 ×). (B) *In vitro* swelling ratio curves of the hydrogel under 24 and 37 °C conditions. (C) *In vitro* degradation

CCUG 58541 on Columbia blood agar, *C. albicans* ATCC 10231 on Sabouraud dextrose agar, and *C. krusei* ATCC 6258 on YM agar, all at a concentration of $1 \times 10^5$ CFU/mL. After plating, plates were dried for 5 min. Drug-loaded hydrogels were incubated in 2 mL PBS at 37 °C, with supernatant collected on Days 1, 3, 5, and 7. The free drug group consisted of an equivalent concentration of drug-loaded hydrogel release. The following groups were tested: drug-loaded hydrogel, free drug, blank hydrogel (no drug or $Zn^{2+}$), $Zn^{2+}$-crosslinked hydrogel (no drug, with $Zn^{2+}$), and saline control. A 100 μL sample from each group was added to the paper discs on the inoculated plates. Bacterial plates were incubated at 37 °C for 24 h, and fungal plates at 30 °C for 48 h. Inhibition zone diameters were measured at different time points.

### 2.15. Scratch assay

Blank and drug-loaded hydrogels were incubated in F-12K medium with 10% FBS at 37 °C for 24 h. The supernatant was collected, filtered through a 0.22 μm membrane, and used as the hydrogel release medium. HUC cells were seeded in 12-well plates to 90% confluence, then scratched with a sterile 200 μL pipette tip. After removing floating cells, the medium was replaced according to experimental groups: blank, blank hydrogel, and drug-loaded hydrogel. Scratch images were captured at 0, 12, and 24 h, and migration was analyzed using ImageJ software.

### 2.16. Flow cytometry (apoptosis, mitochondrial membrane potential, and ROS levels)

HUC cells were treated for 24 h, followed by assessment of apoptosis (Annexin V-FITC/PI), mitochondrial membrane potential (JC-1), and ROS (DCFH-DA). For apoptosis, cells were stained with Annexin V-FITC/PI and incubated for 15 min in the dark. Mitochondrial membrane potential was measured by incubating with JC-1 at 37 °C for 30 min. ROS was assessed using 10 μmol/L DCFH-DA. Samples were analyzed by flow cytometry (BD FACSCalibur or Beckman CytoFLEX) and data processed using CytExpert and FlowJo.

### 2.17. UTIs mouse model and treatment groups

Female C57BL/6 mice (6−8 weeks, 18−22 g) were used to establish bacterial and fungal UTIs models. Mice were fasted and water-deprived for 12 h prior to infection. For bacterial infection, *E. coli* (ATCC 25922, $1 \times 10^7$ CFU/mL) was instilled into the bladder, and for fungal infection, *C. albicans* (ATCC 10231, $1 \times 10^6$ CFU/mL) was used. Under 2%−3% isoflurane anesthesia, a PE-10 catheter was inserted into the bladder to inject 100 μL of the suspension. Mice were kept supine for 15 min to ensure proper contact. After catheter removal, mice were allowed to recover. Infection was confirmed by monitoring behavior and urine CFU counts, with successful infection defined as $\geq 1 \times 10^4$ CFU/mL.

Mice were then randomly assigned to five groups: 1) control (no infection or treatment), 2) infected (no treatment), 3) free drug, 4) blank hydrogel, and 5) drug-loaded hydrogel. After 12-h fasting, each group received 50 μL of treatment *via* catheter, retained for 15 min. After 7 days, mice were euthanized and bladder and kidney tissues collected. Some samples were fixed for transmission electron microscopy (TEM) and IHC analysis, while others were stored at −80 °C. Serum and urine samples were also collected and stored at −80 °C.

### 2.18. Urine spot assay

Mice were placed individually in sterile cages lined with 125 mm filter paper (Whatman International Ltd., Maidstone, England) and allowed to move freely for 1 h. The filter paper was then removed and urine spots were imaged by the Bio-Rad ChemiDoc MP system. Image analysis was performed with ImageJ software to quantify the number and area of urine spots, assessing micturition frequency.

### 2.19. Leukocyturia and inflammatory cytokine measurement

Urine samples were collected before infection, after infection, and on Days 1, 3, 5, and 7 post-treatment. A 10 μL aliquot was placed on a slide, covered with a coverslip, and examined under a microscope to manually count leukocytes. Serum from mice in different groups was collected, and levels of alpha tumor necrosis factor (TNF-$\alpha$), IL-6, and CRP were measured using commercial ELISA kits (FineTest, China), following the manufacturer's instructions.

### 2.20. Hematoxylin−eosin staining

Bladder tissue was fixed in 4% paraformaldehyde, dehydrated using a fully automated machine (JT-12S, China) with a graded ethanol series, and embedded in paraffin (BMJ-A, China). Sections were cut with a rotary microtome (Leica, Germany), deparaffinized with xylene, rehydrated through graded ethanol, and immersed in ultrapure water for 5 min. The sections were stained with hematoxylin, washed, differentiated in hydrochloric acid alcohol, washed again, and then returned to blue in 50 °C warm water or a weak alkaline solution. After washing, they were treated with 85% ethanol, eosin stained, washed, air-dried, and mounted.

behavior of the hydrogel over 8 days at 24 and 37 °C. (D) *In vivo* degradation of the hydrogel in mice over 7 days. (E) *In vivo* imaging of small animals showing changes in fluorescence signals from bladder-retained hydrogel on Days 1, 3, 5, 7, and 9. (F) Quantitative analysis of fluorescence intensity over time. (G) Schematic diagram of the *in vitro* cumulative drug release experiment. (H) *In vitro* cumulative release curve of levofloxacin. (I) *In vitro* cumulative release curve of fluconazole. (J) Schematic diagram of the *in vivo* drug release experiment. (K) *In vivo* release profile of levofloxacin on Days 1, 3, 5, and 7, based on urinary drug concentrations (OD = 291, $n = 6$). (L) *In vivo* release profile of fluconazole on Days 1, 3, 5, and 7, based on urinary drug concentrations (OD = 261, $n = 6$). (M) Release profile of levofloxacin and fluconazole in healthy human urine environment (37 °C, $n = 3$). (N) Time-concentration curve and AUC of levofloxacin in urine of C57BL/6 mice after hydrogel instillation ($n = 3$). (O) Time−concentration curve and AUC of fluconazole in urine of C57BL/6 mice after hydrogel instillation ($n = 3$). (P) Time−concentration curve of fluconazole and levofloxacin in bladder of C57BL/6 mice after hydrogel instillation ($n = 3$). (Q) Time−-concentration curve of fluconazole and levofloxacin in the serum of C57BL/6 mice after hydrogel instillation ($n = 3$). Abbreviations: AUC, area under the curve; FCZ, fluconazole; Hgel, hydrogel; LFX, levofloxacin; OD, optical density; PBS, phosphate-buffered saline; SEM, scanning electron microscope; UPLC−MS/MS, ultra performance liquid chromatography tandem mass spectrometry. $^*P < 0.05$, $^{**}P < 0.01$, $^{***}P < 0.001$; ns, not significant.

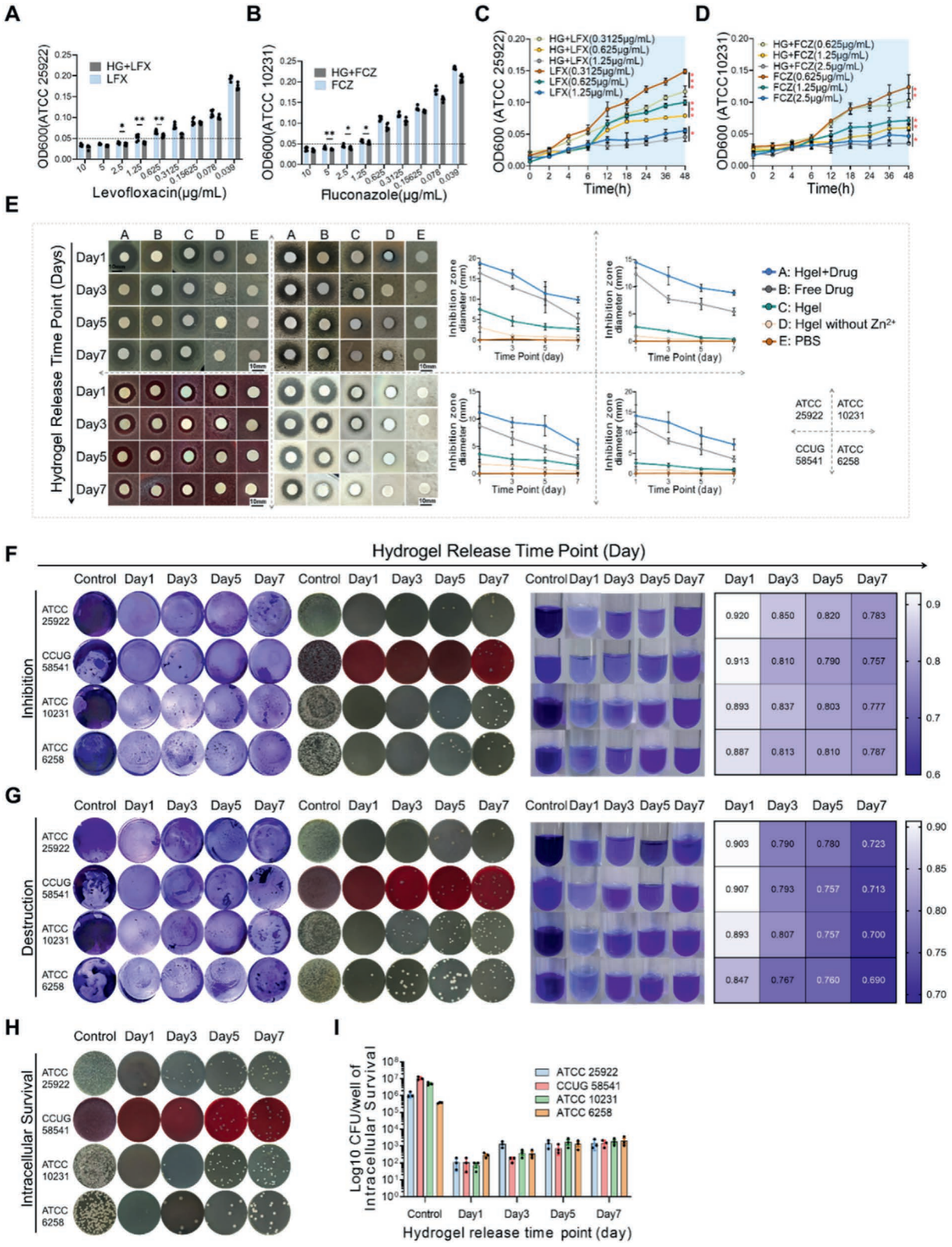


**Figure 3** Evaluation of drug-loaded hydrogels: antibacterial, biofilm inhibition, and intracellular survival. (A, B) MIC ranges of drug-loaded *vs.* free levofloxacin (A) and fluconazole (B) against *E. coli* and *C. albicans*. (C, D) Sustained antibacterial effects of levofloxacin (C) and fluconazole (D) hydrogels against *E. coli* and *C. albicans* over extended incubation. (E) Representative inhibition zone images and diameters after 24-h co-culture at Days 1, 3, 5, and 7 of *E. coli* ATCC 25922, *E. coli* CCUG 58541, *C. albicans* ATCC 10231, and *C. krusei* ATCC 6258 in different treatment groups (drug-loaded hydrogel, free drug, blank hydrogel, hydrogel without $Zn^{2+}$, and PBS). (F, G) Biofilm inhibition and disruption of *E. coli* ATCC 25922, *E. coli* CCUG 58541, *C. albicans* ATCC 10231, and *C. krusei* ATCC 6258 by hydrogel release solutions at different time

### 2.21. Immunohistochemistry (IHC)

IL-6 and TNF-$\alpha$ expression in bladder and kidney tissues was assessed by immunohistochemistry. Tissues were fixed in 4% paraformaldehyde, paraffin-embedded, and sectioned at 4 μm. Sections were deparaffinized, rehydrated, and subjected to antigen retrieval in citrate buffer (pH 6.0) at 80 °C for 20 min. Endogenous peroxidase activity was blocked with 3% hydrogen peroxide for 10 min, followed by PBS washing. After blocking with normal goat serum, sections were incubated overnight at 4 °C with primary antibodies (anti-IL-6, anti-TNF, 1:200). HRP-conjugated secondary antibodies were applied and incubated at 37 °C for 30 min. DAB was used for visualization, and the reaction was terminated with distilled water. Sections were counterstained with hematoxylin, dehydrated, and mounted. Images were captured with a Motic BA410 microscope and analyzed using ImageJ to quantify the positive staining area and calculate the percentage of positive expression for IL-6 and TNF in the tissues.

### 2.22. TEM

Bladder and kidney tissues from mice were collected on Day 7 post-treatment for TEM analysis. Tissue blocks (approximately 1 $mm^3$) were fixed in 2.5% glutaraldehyde for 12 h and 1% osmium tetroxide for 1.5 h at 4 °C. Samples were dehydrated through a graded acetone series (30%−100%) and infiltrated with a 3:1, 1:1, and 1:3 mixture of acetone and Epon-812 resin, followed by pure Epon-812 embedding and polymerization at 60 °C for 48 h. Semi-thin sections were cut for light microscopy localization using a Leica UC7 ultramicrotome, selecting the bladder mucosal and renal pelvic epithelial regions. Ultrathin sections (60−90 nm) were collected on copper grids and stained with uranyl acetate (10−15 min) and lead citrate (1−2 min). Imaging was performed with a JEOL JEM-1400FLASH transmission electron microscope at magnifications of 8000−30,000×. Ultrastructural changes in the bladder and kidney, including cell integrity, organelle morphology, and tissue pathology, were assessed. Autophagic clearance efficiency is calculated as Eq. (4):

$$\text{Autophagic clearance efficiency}\,(\%) = \text{Number of fully degraded autolysosomes}/\text{Total number of autophagic structures}) \times 100 \quad (4)$$

The total number of autophagic structures refers to the sum of autophagosomes, autophages, and autolysosomes. Autolysosome maturity is calculated as Eq. (5)

:

$$\text{Autolysosome maturity}\,(\%) = [\text{Number of mature autolysosomes} / (\text{autophagosomes} + \text{autophages} + \text{autolysosomes})] \times 100 \quad (5)$$

This means the maturity of autolysosomes is assessed by the proportion of typical mature autolysosomes (single-membrane, degraded contents) in the total autophagic structures.

### 2.23. Transcriptome sequencing

Bladder tissues from normal, infection, and drug-loaded hydrogel treatment groups of mice ($n = 3$) were collected for total RNA extraction and transcriptome sequencing. RNA quality was assessed using NanoDrop and Agilent 5300, and samples meeting library construction standards were used for mRNA enrichment using Oligo(dT) magnetic beads. Libraries were constructed and sequenced on the NovaSeq X Plus or DNBSEQ-T7 platforms with PE150 read length. Raw data were quality controlled using fastp, then aligned to the mouse reference genome (GRCm38/mm10) using HISAT2, and expression levels were normalized to FPKM. Subsequent analyses included PCA, heatmap and volcano plot visualizations, Gene Ontology (GO)/Kyoto Encyclopedia of Genes and Genomes (KEGG)/Reactome pathway enrichment, GSEA gene set enrichment analysis, protein-protein interaction network construction, and immune cell infiltration analysis based on CIBERSORT. These analyses aimed to evaluate the roles of drug-loaded hydrogel in gene regulation, signaling pathway modulation, and immune microenvironment remodeling.

### 2.24. Western blotting

Bladder tissues were collected from mice and lysed with RIPA buffer containing protease and phosphatase inhibitors. The tissues were homogenized on ice, lysed for 30 min, and centrifuged at 12,000×$g$ for 15 min at 4 °C to collect the supernatant. Protein concentration was measured using the BCA assay. Equal protein amounts were separated by SDS-PAGE, transferred to PVDF membranes, and blocked with 5% non-fat milk for 1 h. Membranes were incubated overnight at 4 °C with primary antibodies (LC3, p62, p-ULK1, ATG5, ULK1, PINK1, Parkin, GAPDH, Tomm20, Tomm70). After washing, membranes were incubated with fluorescently labeled secondary antibodies for 1 h at room temperature and fluorescence was detected using an imaging system. Images were analyzed using ImageJ software for grayscale intensity.

### 2.25. Data analysis

Statistical analyses were performed using GraphPad Prism v.9.5.1. Two-way ANOVA followed by Tukey's *post hoc* test was used for comparing treatment effects across time points. For comparisons between two groups, an unpaired two-tailed Student's *t*-test was used. Survival curves were analyzed using the log-rank (Mantel−Cox) test. Data are presented as mean ± standard deviation (SD). $^*P < 0.05$, $^{**}P < 0.01$, $^{***}P < 0.001$.

points. (F) Inhibition assay of biofilm formation by hydrogel release solutions. (G) Disruption assay of pre-formed biofilms by hydrogel release solutions. From left to right: representative crystal violet biofilm images, viable biofilm cell counts, crystal violet-ethanol solubilization images, and biofilm inhibition/disruption rate analysis. (H, I) Intracellular bacterial survival of *E. coli* ATCC 25922, *E. coli* CCUG 58541, *C. albicans* ATCC 10231, and *C. krusei* ATCC 6258 treated with hydrogel release solutions at different time points. (H) Representative images of viable intracellular bacterial counts after hydrogel release solution treatment. (I) Quantification of viable intracellular bacteria at different time points following hydrogel release solution treatment. Abbreviations: ATCC, American Type Culture Collection; *C. albicans*, *Candida albicans*; CCUG, Culture Collection University of Gothenburg; *C. krusei*, *Candida krusei*; *E. coli*, *Escherichia coli*; FCZ, fluconazole; Hgel, hydrogel; LFX, levofloxacin; MIC, minimum inhibitory concentration; PBS, phosphate-buffered saline. $^*P < 0.05$, $^{**}P < 0.01$, $^{***}P < 0.001$; ns, not significant.

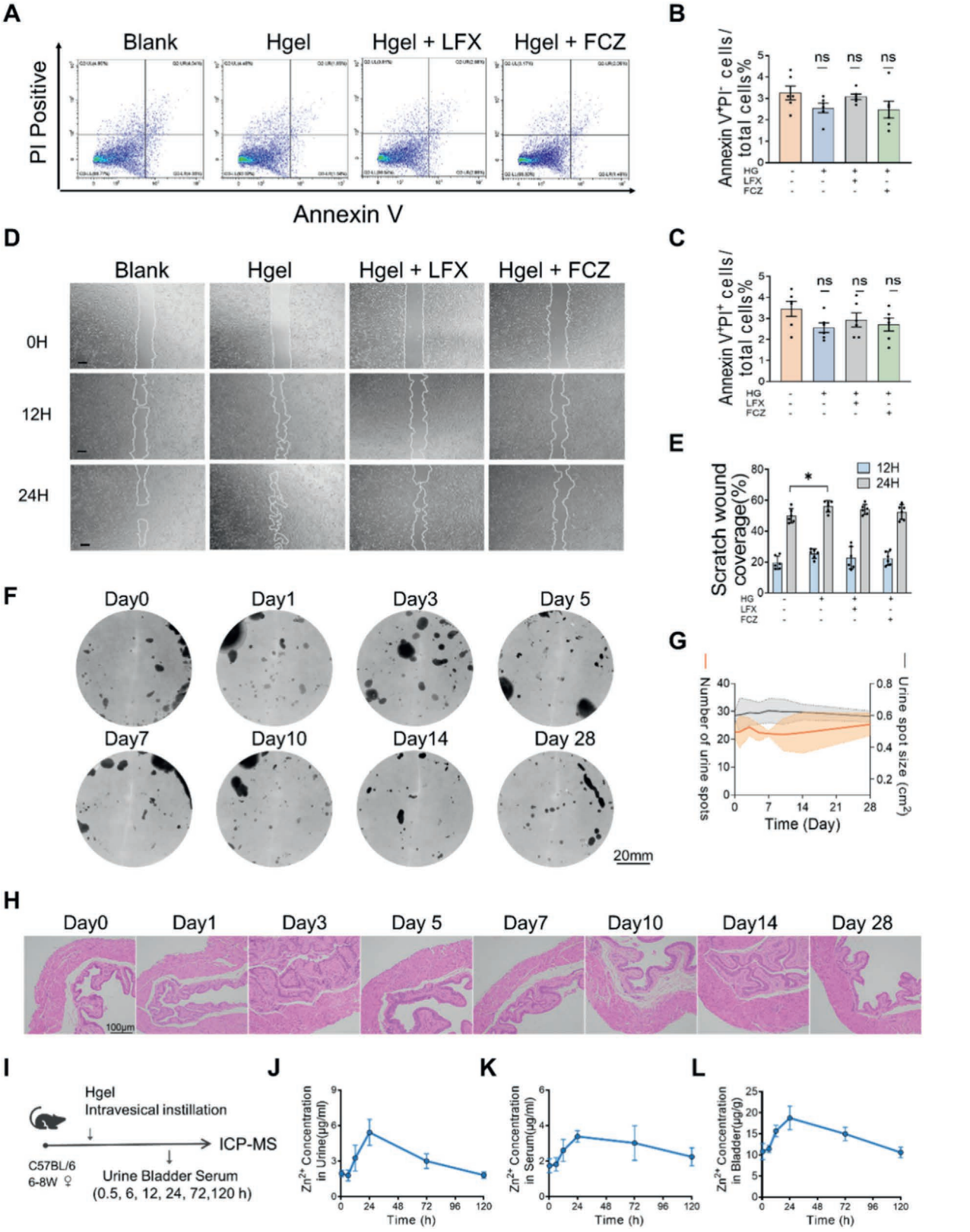


**Figure 4** Safety evaluation of drug-loaded hydrogels. (A−C): Flow cytometric analysis of apoptosis in HUCs following 24 h exposure to blank hydrogel, levofloxacin-loaded hydrogel, fluconazole-loaded hydrogel, and PBS control. (A) Representative flow cytometry plots; (B, C) Quantification of early (B) and late (C) apoptosis. (D, E) HUC migration assessed by scratch assay at 12 and 24 h. (D) Representative scratch images (scale bar = 200 μm); (E) Quantitative analysis of scratch closure. (F, G) Urine spot assay in mice following bladder infusion of hydrogels at Days 1, 3, 5, 7, 10, 14, and 28. (F) Representative urine spot images. (G) Quantification of spot size and number. (H) HE staining of bladder tissue

## 3. Results

### 3.1. Synthesis, optimization, and performance characterization of DRIVER

$NaIO_4$ oxidation introduced aldehyde groups into HA, modulating the hydrogel's crosslinking density and dynamic properties. OHA and NOCC form a dynamic covalent network *via* a Schiff base reaction, with $Zn^{2+}$ inducing coordination crosslinking between NOCC molecules, resulting in a synergistic crosslinked structure (Fig. 1A). The combination of dynamic covalent bonding and metal coordination mechanism enhances the hydrogel's stability and responsiveness. Gelation behavior and time are influenced by factors such as OHA and NOCC concentrations, their ratios, and the oxidation degree of OHA. Under simulated injection conditions, the impact of component ratios on gelation behavior (precipitation, gelation, or sol state) and gelation time was assessed to determine an optimal parameter window for excellent injectability and gelation properties (Fig. 1B, Supporting Information Fig. S1A and S1B). Based on gelation performance and practical requirements, the subsequent experiments selected 40% oxidized OHA (20 mg/mL) and NOCC (20 mg/mL) as the optimal combination, which was mixed in a volume ratio of 20:80:2 with $ZnCl_2$ (10 mg/mL). $^1$H NMR spectroscopy revealed that the oxidation treatment modified the chemical environment of the hydroxyl groups on HA, enabling dynamic covalent crosslinking with NOCC (Supporting Information Figs. S2 and S3). FTIR spectroscopy revealed a characteristic C═O stretch in OHA and confirmed $-NH_2$ and $-COOH$ groups in NOCC, supporting the formation of dynamic covalent C═N linkages (Fig. 1C–E). Rheological profiling showed that the hydrogel exhibited low initial modulus for facile catheter injection, followed by time-dependent stiffening into a mechanically stable gel (Fig. 1F). Drug incorporation further enhanced viscoelasticity, supporting prolonged bladder retention and dynamic physiological adaptability (Fig. 1G and H).

### 3.2. DRIVER's stable porous structure ensures efficient drug release

SEM revealed a uniformly interconnected porous architecture in DRIVER (porosity 50%−55%), enabling rapid solute transport and efficient stress dissipation while preserving structural fidelity after drug loading (Fig. 2A, Supporting Information Fig. S4A and S4B). The $Zn^{2+}$-crosslinked hydrogel swelled by ∼300% at 37 °C within 12 h, supporting an initial burst release phase (Fig. 2B). Both *in vitro* and *in vivo* studies demonstrated that the hydrogel maintained structural stability for 7−9 days (Fig. 2C–F). Approximately 60% of levofloxacin and 50% of fluconazole were released within the first 48 h, providing early antimicrobial coverage (Fig. 2G–I). The drug was still detectable in urine 7 days after instillation, aligning with clinical treatment timescales for UTIs (Fig. 2J–L). Comparable release kinetics were observed in human urine at physiological temperature (Fig. 2M). Pharmacokinetic profiling in mice showed urinary peak concentrations of levofloxacin and fluconazole at 24−48 h (36 and 50 μg/mL, respectively), with 7-day area under the curve values of 2249 ± 156.1 μg·h/mL and 3259 ± 168.1 μg·h/mL (Fig. 2N–O). Drug levels in bladder tissue and serum paralleled the urinary time course but remained minimal, indicating that released agents were largely confined to the infection site (Fig. 2P and Q).

### 3.3. DRIVER exhibits potent activity against planktonic, biofilm, and intracellular pathogens

DRIVER substantially enhanced antimicrobial efficacy across bacterial and fungal models. Encapsulation lowered the MIC of levofloxacin against *E. coli* to 0.625−1.25 μg/mL and that of fluconazole against *C. albicans* to 1.25−2.5 μg/mL (Fig. 3A and B). Moreover, DRIVER maintained superior suppression of microbial growth over time, as evidenced by consistently lower $OD_{600}$ values throughout the co-incubation period (Fig. 3C and D). To capture the clinical heterogeneity and resistance profiles of urinary pathogens, we included levofloxacin-resistant *E. coli* CCUG 58541 and fluconazole-resistant *C. krusei* ATCC 6258. At equivalent time points, DRIVER generated larger inhibition zones than the free drug control (Fig. 3E) and consistently lower $OD_{600}$ values (Supporting Information Fig. S5A–S5D). The incorporation of $Zn^{2+}$ crosslinking further potentiated this antimicrobial activity. For susceptible strains, DRIVER (50 μL) loaded with only 6.25−25 μg of drug produced strong inhibition, and at higher loads of 50−200 μg it remained effective against resistant pathogens, demonstrating preserved potency against clinically relevant resistance phenotypes (Supporting Information Fig. S6A–S6D).

Biofilm formation on the urothelium allows bacterial and fungal pathogens to evade immune clearance and develop heightened antibiotic tolerance, driving persistent and recurrent infections. DRIVER loaded with 1.6 mg/mL of drug suppressed biofilm formation in resistant strains by approximately 80%, reaching up to 98%, and induced ∼90% biofilm disruption at the 3.2 mg/mL load with marked reductions in viable cells (Supporting Information Fig. S7A–S7D). Release media from DRIVER containing 100 μg of levofloxacin or 150 μg of fluconazole per 50 μL hydrogel maintained strong antibiofilm activity for one week; on Day 7, inhibition remained above 75% and disruption approached 70%, accompanied by pronounced reductions in viable pathogens (Fig. 3F and G, Supporting Information Fig. S8A and S8B). Because intracellular epithelial colonization fuels recurrence, we evaluated DRIVER in an intracellular infection model. Across all time points within the one-week release window, DRIVER suppressed intracellular bacterial proliferation, indicating that sustained release effectively counters intracellular persistence (Fig. 3H and I).

### 3.4. Biocompatibility and in vivo safety of DRIVER hydrogels

Co-culture of HUCs with either blank or drug-loaded hydrogels for 24 h induced no detectable apoptosis, demonstrating excellent biocompatibility (Fig. 4A−C). Notably, blank hydrogels enhanced HUC migration, suggesting an intrinsic capacity to support

in mice at Days 1, 3, 5, 7, 10, 14, and 28 post-hydrogel infusion. (I−L) Measurement of zinc ion concentrations in urine, blood, and bladder at 0.5, 6, 12, 24, 72, and 120 h post-hydrogel infusion. (I) Experimental schematic. (J) Urinary zinc ion concentration−time curve following hydrogel infusion; (K) Plasma zinc ion concentration−time curve following hydrogel infusion. (L) Bladder zinc ion concentration−time curve following hydrogel infusion. Abbreviations: FCZ, fluconazole; HE, Hematoxylin-Eosin; HG, hydrogel; Hgel, hydrogel; HUC, human urethral epithelial cells; LFX, levofloxacin; PBS, phosphate-buffered saline; PI, propidium iodide. $*P < 0.05$, $**P < 0.01$, $***P < 0.001$; ns, not significant.

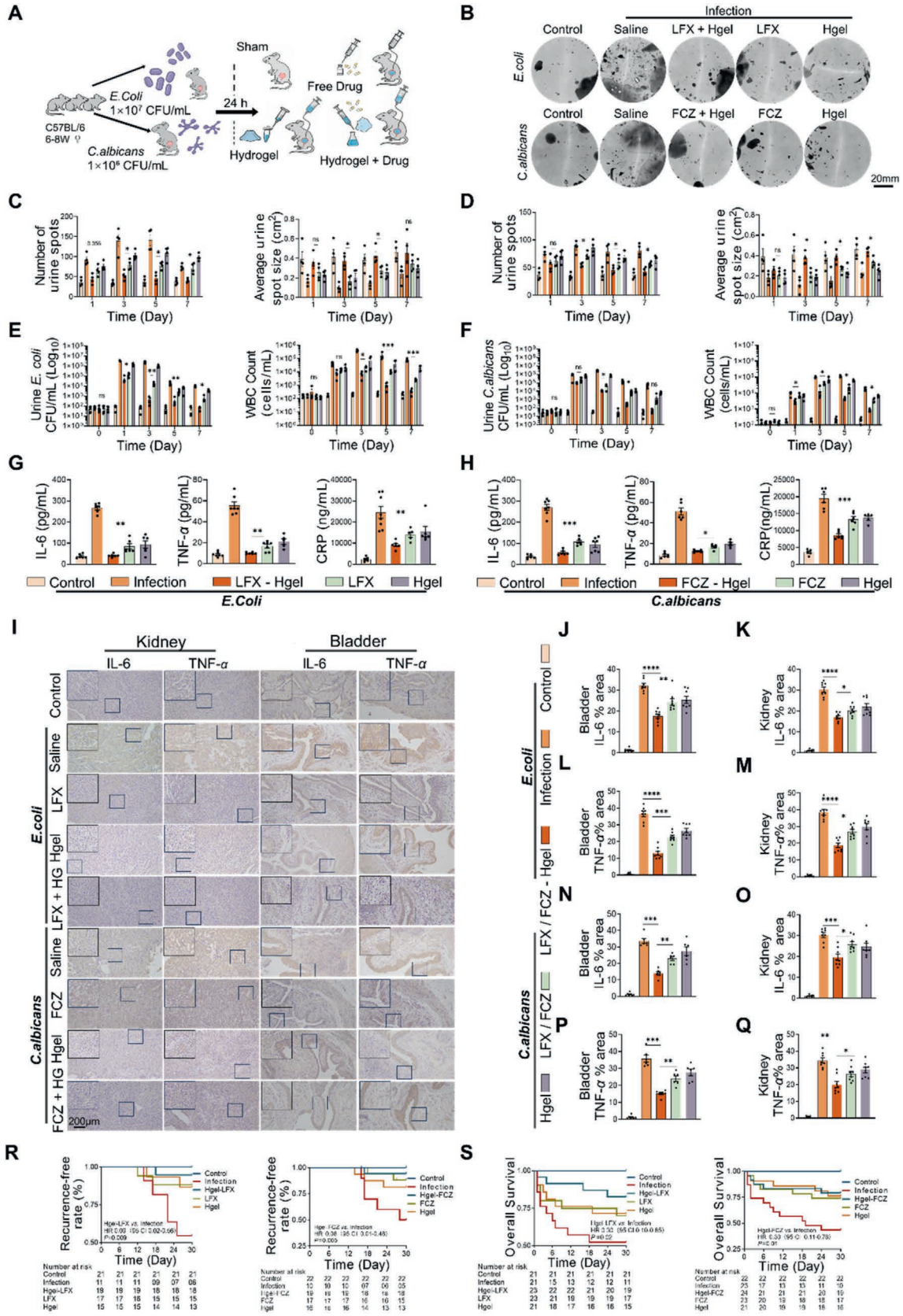


**Figure 5** *In vivo* therapeutic effect of drug-loaded hydrogels in bacterial and fungal UTIs models. (A) Schematic of UTIs model establishment and treatment regimen. (B) Representative urine spot images. (C) Urine spot number and area in the bacterial infection group on Days 1, 3, 5, and 7. (D) Urine spot number and area in the fungal infection group at the corresponding time points. (E) Dynamics of *E. coli* CFU and urine leukocyte counts in mouse urine at Days 1, 3, 5, and 7 across different treatment groups (*E. coli* infected, non-infected, hydrogel, drug-loaded

epithelial repair (Fig. 4D and E). Given the hydrogel's prolonged intravesical residence (>1 week), we assessed its long-term impact on bladder physiology. Following 28 days of intravesical retention in C57BL/6 mice, voiding frequency and urine volume remained unchanged, indicating preserved bladder function (Fig. 4F and G). Histological analyses across all time points (Days 1, 3, 5, 7, 10, 14, and 28) showed intact urothelial architecture without inflammation or fibrosis (Fig. 4H).

Because $Zn^{2+}$ may pose tissue toxicity, we quantified $Zn^{2+}$ levels in urine, serum, and bladder tissue (Fig. 4I). $Zn^{2+}$ concentrations remained stable over 5 days post-instillation. Although a transient peak appeared at 24 h (urine: 5.4 μg/mL; serum: 3.4 μg/mL; bladder: 18.7 μg/g), all values were within the safe range and declined rapidly thereafter, with no evidence of $Zn^{2+}$ accumulation (Fig. 4J−L).

### *3.5. DRIVER provides effective treatment of bacterial and fungal UTIs*

Female C57BL/6 mice (6−8 weeks) were used to establish *E. coli* ($1 \times 10^7$ CFU/mL) and *C. albicans* ($1 \times 10^6$ CFU/mL) UTIs models *via* bladder instillation. Infected mice exhibited typical symptoms including urinary irritation, weight loss, elevated urinary leukocytes, and pathogen loads above diagnostic thresholds ($>1 \times 10^4$ CFU/mL) (Supporting Information Figs. S9−S11). At 24 h post-infection, serum TNF-α, IL-6, and CRP levels were significantly elevated, alongside urine acidification in the *E. coli* group (Supporting Information Figs. S12 and S13). Upon infection confirmation, mice were randomized into four treatment arms: sham, free drug, blank hydrogel, and drug-loaded hydrogel (Fig. 5A).

In the bacterial infection model, drug-loaded hydrogel reduced urinary spot number by 50% on Day 1 and doubled spot area, indicating relief of urinary frequency and restoration of bladder function (Fig. 5B and C). In fungal infections, urine spot reduction became significant by Day 3 (Fig. 5B and D). Pathogen burden decreased by 3.4 log units for *E. coli* and 2.3 log units for *C. albicans* by Day 3, and the fungal burden further declined to 3.2 log units by Day 7 in the drug-loaded hydrogel group (Fig. 5E and F). Leukocyte counts were ∼70% lower than the free drug group by Day 3.

In *E. coli* infection, serum IL-6, TNF-α, and CRP levels were reduced by 49%, 41%, and 35%, respectively, relative to free drug (Fig. 5G), with similar inhibition in fungal UTIs (Fig. 5H). Immunohistochemistry revealed reduced IL-6 and TNF expression in both bladder and kidney tissues in the hydrogel group (Fig. 5I). In *E. coli* infection, bladder IL-6 and TNF were reduced by 46% and 68%, kidney levels by 42% and 51%, respectively (Fig. 5J−M). In *C. albicans* infection, reductions were 55% (IL-6) and 35% (TNF) in bladder, and 55% and 42% in kidney (Fig. 5N−Q). During a 30-day follow-up, recurrence rates were significantly lower in the hydrogel group (Fig. 5R), with body weight recovery between Days 20−30 markedly superior to free drug (Supporting Information Fig. S14A and S14B). Survival was also improved: hazard ratio (HR) = 0.30 (95% CI: 0.10−0.85, $P = 0.02$) in bacterial UTIs and HR = 0.30 (95% CI: 0.11−0.78, $P = 0.01$) in fungal UTIs (Fig. 5S).

### *3.6. Regulatory effects of DRIVER on gene expression and immunity in UTIs*

RNA sequencing revealed that DRIVER modulates transcriptional programs associated with infection and tissue homeostasis, with heatmap clustering and principal component analysis (PCA) showing that the treatment group transcriptionally resembled healthy controls (Fig. 6A and B). Venn analysis identified 160 differentially expressed genes shared across all groups (Fig. 6C). Infection induced upregulation of genes related to inflammation and interferon signaling, whereas treatment elevated genes associated with tissue repair and homeostasis, including Ngf, Timp1, and Fos, indicating potential reversal of infection-induced transcriptional changes (Fig. 6D and E).

GO enrichment analysis showed that the differentially expressed genes were primarily involved in functional modules such as "regulation of activated T cell proliferation", "wound healing", "oxidoreductase activity" and "endosome" (Fig. 6F). KEGG pathway enrichment analysis revealed pathways related to "ECM-receptor interactions", "PI3K-Akt signaling pathway" and "cytokine-cytokine receptor interaction", suggesting that the hydrogel may promote tissue repair by activating autophagy (Fig. 6G). Reactome analysis revealed significant enrichment in pathways such as "bio-oxidation" and "mitochondrial translation elongation" along with PI3K-AKT negative regulation and collagen synthesis modification pathways, suggesting the hydrogel's role in mitochondrial function, energy metabolism, and tissue repair (Supporting Information Figs. S15 and S16). Protein-protein interaction network analysis showed that differentially expressed genes were concentrated in mitochondrial complex I subunits (*e.g.*, Ndufa1, Ndufb7, Ndufs6), indicating that hydrogel treatment stabilizes the mitochondrial electron transport chain to enhance metabolic efficiency (Fig. 6H). Gene set enrichment analysis (GSEA) further confirms that drug-loaded hydrogel treatment enhances mitochondrial protein synthesis and maintains electron transport chain activity (Fig. 6I−L, Supporting Information Fig. S17A and S17B). Additionally, autophagy and endocytosis-related genes showed an upregulation trend (Fig. S17C and S17D). Immune cell infiltration analysis showed that the drug-loaded hydrogel enhanced $CD8^+$ T cell, NK cell, memory B cell, and T cell infiltration while inhibiting monocyte and neutrophil infiltration, promoting the remodeling of the

hydrogel, free drug). (F) Dynamics of *C. albicans* CFU and urine leukocyte counts in mouse urine at Days 1, 3, 5, and 7 across different treatment groups (*C. albicans* infected, non-infected, hydrogel, drug-loaded hydrogel, free drug). (G) Analysis of serum levels of IL-6, TNF-α, and CRP in non-infected, infected, hydrogel, drug-loaded hydrogel, and free drug groups in the bacterial infection model. (H) Analysis of serum levels of IL-6, TNF-α, and CRP in different groups in the fungal infection model. (I) Representative immunohistochemical staining of IL-6 and TNF-α in bladder and kidney tissues. (J−M) Quantification of IL-6 and TNF-α positive areas in bladder (J, L) and kidney (K, M) in bacterial UTIs model. (N)−(Q) Quantification of IL-6 and TNF-α expression in bladder (N, P) and kidney (O, Q) in fungal UTIs model. (R) Recurrence analysis of treatment groups in bacterial and fungal UTIs models. (S) Survival analysis of treatment groups in bacterial and fungal UTIs models. Abbreviations: *C. albicans*, *Candida albicans*; CFU, colony-forming units; CRP, C-reactive protein; *E. coli*, *Escherichia coli*; FCZ, fluconazole; Hgel, hydrogel; HR, hazard ratio; IL-6, interleukin-6; LFX, levofloxacin; TNF-α, tumor necrosis factor-alpha; UTIs, urinary tract infections; WBC, white blood cell. $^*P < 0.05$, $^{**}P < 0.01$, $^{***}P < 0.001$; $^{****}P < 0.0001$.

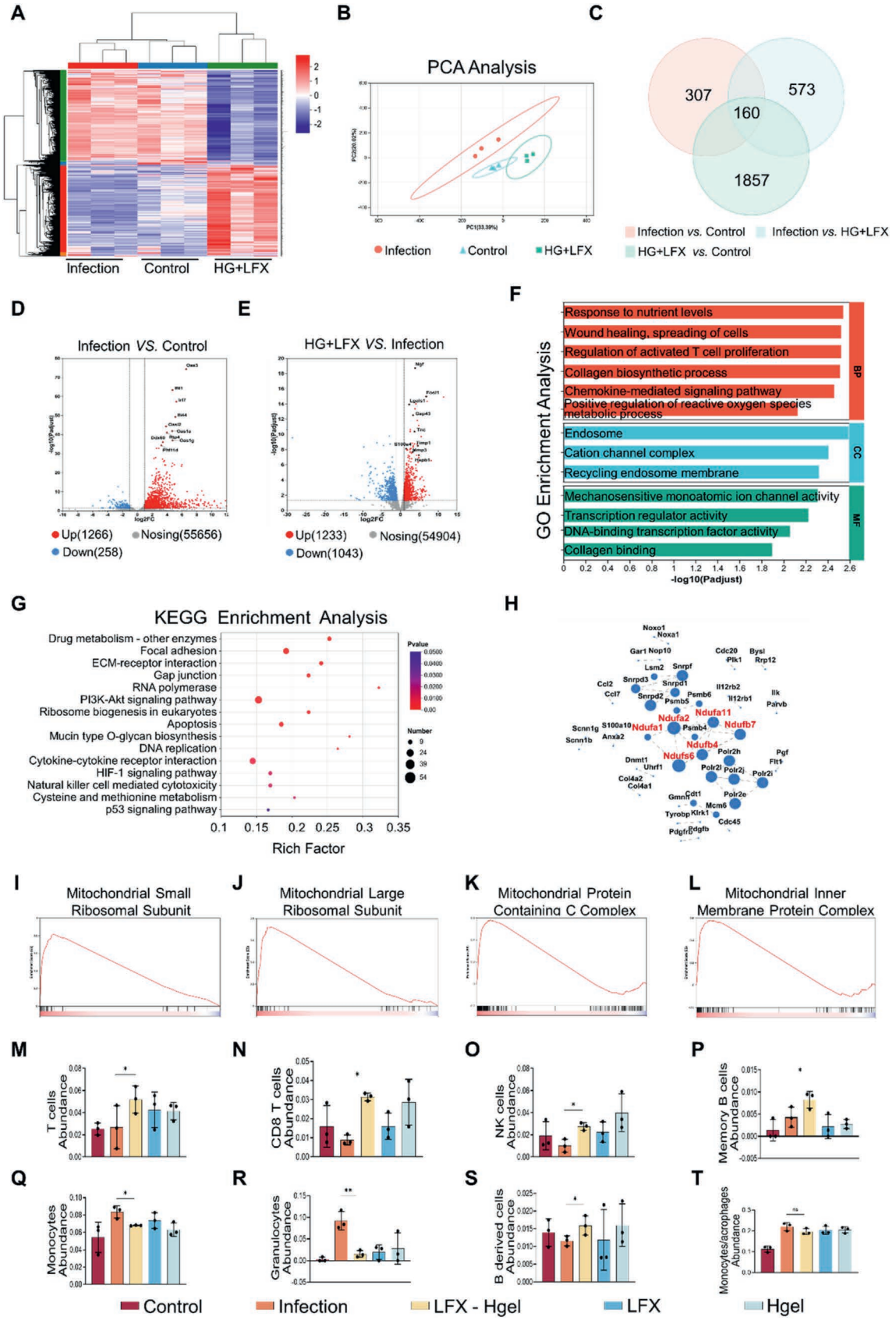


**Figure 6** Transcriptomic profiling identifies potential regulatory mechanisms of drug-loaded hydrogels in UTIs. (A) Heatmap of differentially expressed genes (fold change $\geq 2$, $P < 0.05$) across control, UTIs, and hydrogel-treated groups. (B) PCA illustrating transcriptional clustering among the three groups. (C) Venn diagram of shared and unique DEGs across comparisons. (D, E) Volcano plots showing gene expression

infected microenvironment and restoring immune homeostasis compared to the free antibiotic group (Fig. 6M−T, Supporting Information Fig. S18A−S18H).

### *3.7. DRIVER restores mitochondrial function and autophagy in UTIs*

Infection disrupted epithelial architecture in both the bladder and renal pelvis, with evident nuclear condensation, intercellular gap widening, and mitochondrial swelling. In contrast to the limited protection offered by free drugs, DRIVER treatment preserved epithelial structure and reduced mitochondrial damage, as evidenced by clearer cristae and fewer swollen mitochondria (Fig. 7A−C). Electron-dense double-membrane structures surrounding damaged mitochondria indicated activated mitochondrial autophagy (Supporting Information Figs. S19 and S20), and increased numbers of mature autophagosomes suggested enhanced autolysosomal clearance in both kidney and bladder (Supporting Information Figs. S21 and S22).

Autophagy and mitochondrial homeostasis were further interrogated at the protein level in bladder tissues. Infection triggered canonical autophagy activation, marked by increased LC3-II/LC3-I ratio, elevated p62 levels, and upregulation of ULK1 phosphorylation and ATG5—features indicative of autophagosome accumulation but impaired clearance. DRIVER reversed this dysregulation by lowering p62 expression, promoting LC3 conversion, and further enhancing ULK1 phosphorylation, supporting improved autophagic flux. Notably, PINK1 and Parkin levels were markedly elevated, while TOMM20 expression declined, consistent with mitochondrial autophagy activation and clearance of dysfunctional mitochondria (Fig. 7D−P). In contrast, the free drug group exhibited negligible impact on these pathways. Redox balance and mitochondrial membrane potential were also restored. Flow cytometry revealed that DRIVER suppressed infection-induced ROS accumulation and rescued mitochondrial polarization, as reflected by recovery of the JC-1 red/green fluorescence ratio (Fig. 7Q−T). These results indicate robust attenuation of oxidative stress and preservation of mitochondrial function following hydrogel treatment.

## 4. Discussion

The hydrogel scaffold, DRIVER, developed in this study forms a stable crosslinked network through dynamic covalent bonding and metal coordination, enabling adaptability and responsiveness in the bladder's complex physiological environment. Compared to free drug treatment, the drug-loaded hydrogel exhibited enhanced antibacterial and antifungal activity *in vitro* and *in vivo*, suggesting that its microstructure directly contributes to antimicrobial effects. The hydrogel's local retention and sustained release prolonged drug action, while the synergistic interaction between chitosan derivatives and zinc ions disrupted microbial membranes and metabolic processes, enhancing the anti-infection response. Additionally, the system downregulated inflammatory factors, activated autophagy, and restored mitochondrial function, indicating its role in modulating host-pathogen interactions, local immunity, and tissue homeostasis. Upregulation of autophagy-related genes, inhibition of ROS signaling, and improved mitochondrial function suggest that the hydrogel mitigates oxidative stress, restores metabolic homeostasis, and promotes tissue regeneration. Overall, the hydrogel system not only offers direct anti-infection effects but also supports immune modulation and tissue repair through multiple synergistic mechanisms.

Current hydrogel therapies for UTIs mainly rely on local delivery systems that passively release antimicrobials and do not address the multistage nature of UTIs pathogenesis. Yang et al.[15] used a porcine-derived levofloxacin-loaded decellularized dermal matrix hydrogel to increase local drug levels but did not modulate the immune microenvironment. Guevara et al.[24] developed a PLGA−ciprofloxacin hydrogel in which polymer hydrolysis governs antibiotic release; its rigid network, however, poorly penetrates dense biofilms and lacks immunoregulatory activity. Al-Enizi et al.[25] reported a copper-coordination hydrogel that kills pathogens *via* $Cu^{2+}$-induced oxidative stress, at the risk of impairing bladder epithelial cell viability. Zhang et al.[26] designed a ROS-scavenging hydrogel to limit oxidative damage, yet its stability and antioxidant formulation remain suboptimal. Conventional single-crosslinked hydrogels are also problematic: physically crosslinked networks disintegrate rapidly[27], whereas chemically crosslinked systems often show limited biocompatibility[28]. Dual-crosslinking strategies partially alleviate these issues, as exemplified by the combination of dynamic Schiff base bonds with photochemical crosslinking reported by Wang et al.[29], and the pH-responsive catechol−Fe coordination plus dynamic Schiff base network described by Liang et al[30]. In contrast, The HA/CS−zinc coordination hydrogel developed here combines dynamic covalent bonds with $Zn^{2+}$ coordination to mimic the native mucosal interface, promoting adhesion to injured urothelium. $Zn^{2+}$ disrupts metal homeostasis in uropathogens, enhancing antibacterial efficacy, while chitosan degradation products support macrophage autophagy and reduce pro-inflammatory cytokine production, establishing an antibacterial−anti-inflammatory−pro-regenerative cascade to improve UTIs management. The dual-crosslinked network ensures mechanical stability, maintaining structural integrity in the bladder. Additionally, DRIVER's activity extends beyond planktonic bacteria and fungi to include biofilm-associated and intracellular populations, which have been less explored in previous hydrogel-based UTIs interventions.

Chronicity and recurrence of UTIs result from a cycle of inadequate pathogen clearance, immune imbalance, and impaired tissue repair. Studies have shown that chitosan degradation

changes between Control *vs.* UTIs (D) and UTIs *vs.* hydrogel-treated groups (E). (F) GO enrichment highlighting BP, CC, and MF affected by treatment. (G) KEGG pathway enrichment showing activation of ECM-receptor interaction, PI3K−Akt signaling, and cytokine−cytokine receptor pathways. (H) Protein−protein interaction network identifying mitochondrial complex I subunit enrichment (STRING database). (I−L) GSEA results showing upregulated mitochondrial pathways, including small ribosomal subunits (I), large ribosomal subunits (J), protein-containing complex (K), and inner membrane complexes (L). (M−T) Immune cell infiltration in bladder tissues: T cells (M), $CD8^+$ T cells (N), NK cells (O), memory B cells (P), monocytes (Q), granulocyte (R), B cell-derived populations (S), and monocyte/macrophages (T) across treatment groups. Abbreviations: BP, biological processes; CC, cellular components; GO, Gene Ontology; HG, hydrogel; Hgel, hydrogel; KEGG, Kyoto Encyclopedia of Genes and Genomes; LFX, levofloxacin; MF, molecular functions; PCA, principal component analysis; UTIs, urinary tract infections. $*P < 0.05$, $**P < 0.01$; ns, not significant.

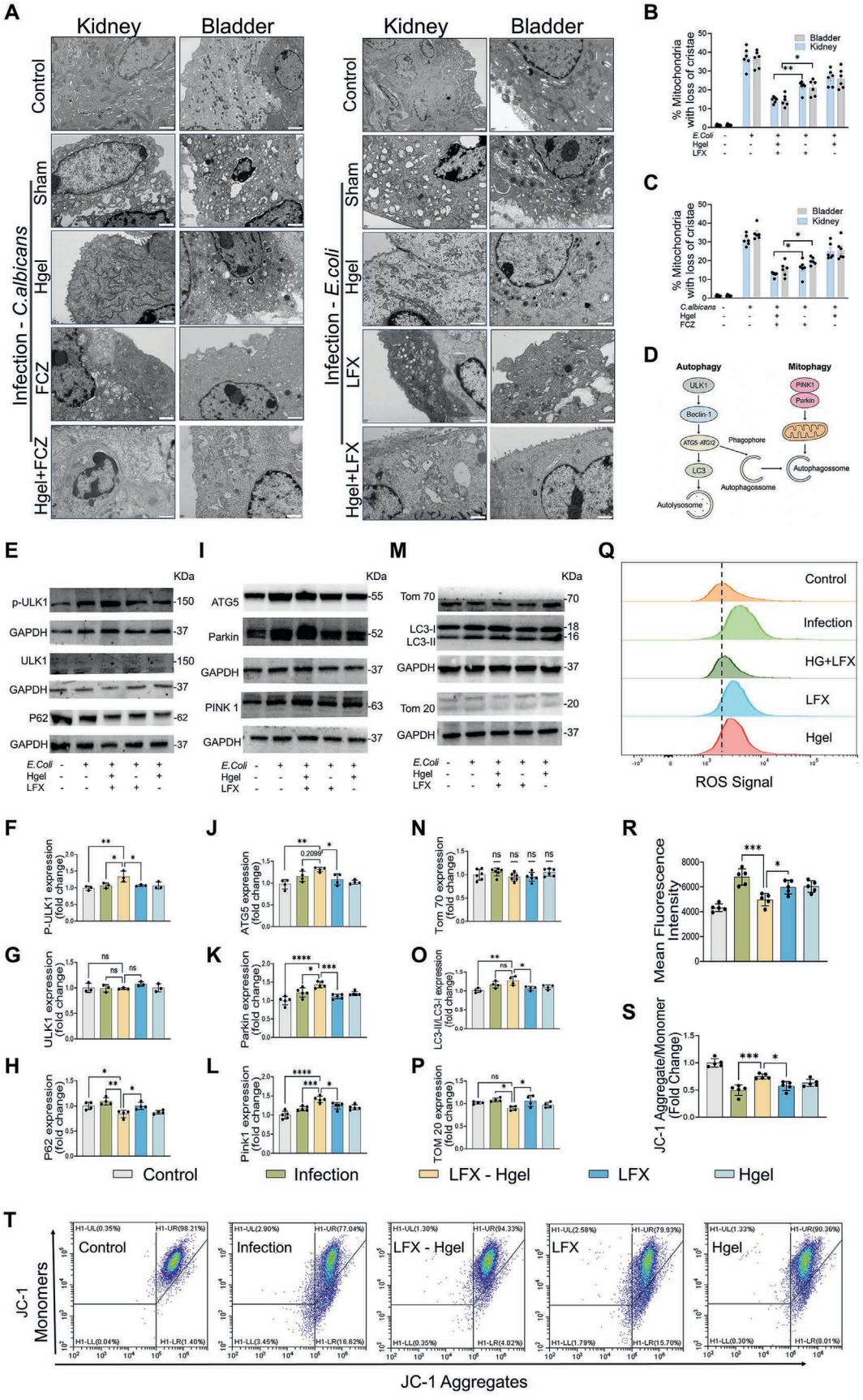


**Figure 7** Analysis of mitochondrial and autophagy regulation in UTIs models. (A) TEM images of kidney and bladder tissues from non-infected, infected, hydrogel, drug-loaded hydrogel, and free drug groups (8000 × ; scale bar: 1 μm). (B, C) Quantification of damaged

products can inhibit excessive inflammation *via* the TLR4/NF-$\kappa$B pathway and induce macrophage autophagy[31]. Chitosan also possesses inherent antimicrobial properties, disrupting bacterial cell membranes through electrostatic interactions with the cell wall[32]. In this study, treatment with the drug-loaded hydrogel significantly reduced IL-6, CRP, and TNF-$\alpha$ levels, while increasing regulatory T cell and B cell infiltration. This suggests that its immune modulation may involve chitosan-mediated TLR4 signaling inhibition and autophagy activation, providing new insights for controlling chronic inflammation in UTIs.

HA, a key component of the extracellular matrix, enhances keratinocyte activity and improves epidermal function by activating CD44 downstream signaling pathways[33]. It promotes epithelial migration and restores tight junction protein ZO-1 expression *via* the CD44 receptor. This, along with the enrichment of ECM-receptor interaction pathways in the transcriptomic data, supports the role of the HA−CD44−PI3K/Akt pathway in mucosal repair, consistent with epithelial barrier dysfunction observed in recurrent UTIs patients[34]. While CD44 overexpression is linked to poor prognosis and treatment resistance in many cancers[35], its moderate activation in inflammation and tissue repair environments aids in tissue repair.

Mutlu's study[36] confirmed that chitosan−zinc complexes are compatible with skin-related cells and exhibit enhanced antimicrobial and anti-inflammatory properties in wound healing. In this study, the slow release of zinc ions aligns with hydrogel degradation, promoting a synergistic effect on multiple biological functions. The sustained release of $Zn^{2+}$ enhances antimicrobial efficiency and is closely associated with mitochondrial function restoration. Previous research suggests that Parkin's catalytic core contains four zinc finger domains, and activation of PINK1 and Parkin may lead to mitochondrial dissociation[37]. The upregulation of mitochondrial electron transport chain genes, increased LC3-II/I ratio of autophagy markers, and reduced ROS levels, combined with $Zn^{2+}$ regulation of the PINK1/Parkin pathway[38-40], indicate that $Zn^{2+}$ may alleviate oxidative stress by stabilizing mitochondrial metabolism and enhancing autophagic clearance. The exact molecular mechanism, however, requires further study.

Excessive zinc ion concentrations can induce cellular toxicity, making it essential to control both the concentration and release rate of zinc, while also conducting long-term biocompatibility assessments. Alsailawi et al.[41] demonstrated that a 60 mg/kg intraperitoneal dose of zinc sulfate induced significant liver degeneration, renal tubular necrosis, neuronal vacuolization, and splenic cell depletion, which represents doses far exceeding the zinc content in our hydrogel (4.79 μg/mouse). In line with established studies on nutritional supplementation, the zinc content in our hydrogel remains within the physiological range (1.5−50 mg/kg)[42,43]. Zinc homeostasis is maintained through rapid systemic buffering and tightly regulated endogenous turnover, ensuring that even with brief, localized exposure to elevated $Zn^{2+}$ levels, circulating zinc remains stable[43]. After DRIVER bladder instillation, serum, urine, and bladder tissue in mice displayed a steady release profile. Additionally, no local inflammation or functional impairment was observed following 28 days of hydrogel instillation. These results, supported by submicroscopic electron microscopy of bladder and kidney tissues, confirm that zinc ion release is controlled and safe.

This hydrogel system has several limitations. While zinc ions are known to enhance antimicrobial efficacy, the direct synergistic effect with antimicrobial agents has not been demonstrated. However, the release pattern of zinc ions aligns with the drug release trend, offering insights into its potential therapeutic mechanism. Future studies will investigate the interaction between zinc ions and antimicrobial agents, particularly in drug-resistant clinical strains. C57BL/6 mice were used to model bacterial and fungal cystitis, simulating human bladder infection pathology and immune responses. The hydrogel's retention, drug release, and tissue response in the bladder were assessed. C57BL/6 mice are highly sensitive to fibrosis and inflammation, mirroring human disease pathophysiology[44,45]. However, differences in bladder structure and function between mice and humans, such as capacity, mucosal thickness, and voiding dynamics, remain. Further validation in large animal models and preclinical studies is needed to confirm clinical translatability and safety.

## 5. Conclusions

We developed DRIVER, a bladder-targeted injectable hydrogel for the precise, long-term treatment of complex and recurrent UTIs. DRIVER combines controlled drug release with local microenvironment modulation through dynamic covalent bonding and metal coordination. Its crosslinking provides mechanical responsiveness and injectability, enabling drug release to match infection progression and adapt to the bladder's dynamic environment. With the synergistic effect of zinc ions and chitosan derivatives, DRIVER enhanced pathogen clearance, biofilm disruption, and intracellular killing in bacterial, fungal, and drug-resistant UTIs models. It also improves urinary symptoms by reducing voiding frequency and increasing micturition volume. Mechanistically, DRIVER regulates mitochondrial function, autophagy, and inflammatory cytokines, boosting antimicrobial defense and tissue repair. Compared to conventional antibiotics, DRIVER offers superior biocompatibility, safety, and controlled release, integrating infection control, immune modulation, and functional restoration into a unified therapeutic approach. This innovative hydrogel system shows strong clinical potential for managing complex and recurrent UTIs, addressing the limitations of current local drug delivery and infection control strategies.

## Acknowledgments

This work was financially supported by the Youth Project of National Natural Science Foundation of China (82200851),

mitochondria in bacterial (B) and fungal (C) UTIs models. (D) Schematic diagram of the mitochondrial autophagy pathway. (E)−(H) Immunoblotting (E) and quantification of p-ULK1 (F), ULK1 (G), and p62 (H) in bladder tissues. (I)−(L) Immunoblotting (I) and quantification of ATG5 (J), Parkin (K), and PINK1 (L). (M)−(P) Immunoblotting (M) and quantification of TOMM70 (N), LC3-II/LC3-I (O), and TOMM20 (P). (Q, R) Flow cytometric analysis of reactive oxygen species (ROS) in HUCs: representative ROS plots (Q) and mean fluorescence intensity (R). (S, T) JC-1-based analysis of mitochondrial membrane potential in HUCs: representative plots (S) and red/green fluorescence ratio (T). Abbreviations: *C. albicans*, *Candida albicans*; *E. coli*, *Escherichia coli*; FCZ, fluconazole; HG, hydrogel; Hgel, hydrogel; LFX, levofloxacin; ROS, reactive oxygen species; TEM, transmission electron microscopy; UTIs, urinary tract infections. $^{*}P < 0.05$, $^{**}P < 0.01$, $^{***}P < 0.001$, $^{****}P < 0.0001$; ns, not significant.

Sichuan Natural Science Foundation for Young Scholars (2023NSFSC1533, China), and Chengdu Key R&D Project (2022-YF05-01510-SN, China).

## Author contributions

Conceptualization: Zhimin Tan, Yu Liu, and Changyang Gong. Methodology: Zhimin Tan, Xinchao Li, and Tao He. Investigation: Zhimin Tan, and Qiyu He. Visualization: Zhimin Tan, and Xinchao Li. Supervision: Zhimin Tan, Yu Liu, Changyang Gong, and Qian Li. Writing-original draft: Zhimin Tan, and Qiyu He. Writing-review & editing: Zhimin Tan, Yu Liu, Changyang Gong, and Qian Li.

## Conflicts of interest

The authors declare no conflicts of interest.

## Appendix A. Supporting information

Supporting Information to this article can be found online at https://doi.org/10.1016/j.apsb.2025.12.048.

## References


1. Bjerklund Johansen TE, Bahrs C, Bruyere F, Cai T, Joseph A, Köves B, et al. Consensus position statement on advancing the classification of patients and tests of cure in studies of antibiotic treatment of complicated urinary tract infections. *Lancet Infect Dis* 2025;**25**: e605−8.
2. Bhuiya S, Kaushik S, Logheeswaran J, Karthika P, Prathiviraj R, Selvin J, et al. Emergence of recurrent urinary tract infection: dissecting the mechanism of antimicrobial resistance, host-pathogen interaction, and hormonal imbalance. *Microb Pathog* 2025;**206**: 107698.
3. Liao WJ, Jiang YH, Jhang JF, Chen SF, Lee YK, Lee CL, et al. Pathophysiology and potential treatment modalities in women with recurrent urinary tract infection. *Tzu Chi Med J* 2025;**37**:117−24.
4. Bi Y, Wang Y, Li W, Chen Y, Qin J, Zheng H. Microbiota analysis of perimenopausal women experiencing recurrent vaginitis in conjunction with urinary tract infection. *BMC Microbiol* 2025;**25**:1.
5. Jousserand N, Auvray F, Chagneau C, Cavalié L, Maurey C, Drut A, et al. Zoonotic potential of uropathogenic *Escherichia coli* lineages from companion animals. *Vet Res* 2025;**56**:69.
6. Sturov NV, Popov SV, Zhukov VA, Lyapunova TV, Rusanova EI, Kobylyanu GN. Intestinal microbiota correction in the treatment and prevention of urinary tract infection. *Turk J Urol* 2022;**48**:406−14.
7. Brigida M, Saviano A, Petruzziello C, Manetti LL, Migneco A, Ojetti V. Gut microbiome implication and modulation in the management of recurrent urinary tract infection. *Pathogens* 2024;**13**:1028.
8. Caplin JD, García AJ. Implantable antimicrobial biomaterials for local drug delivery in bone infection models. *Acta Biomater* 2019;**93**:2−11.
9. Schittkowski MP, Guthoff RF, Drewelow B, Wacke R. Hydrogelexpander as drug delivery system for antibiotics. *Klin Monbl Augenheilkd* 2012;**229**:158−61.
10. Andreev VP, Bushman WA, Weiss JP, Blaivas JG. Dynamic analysis of the voiding patterns in bladder diaries collected in clinical practice. *Neurourol Urodyn* 2025;**44**:707−15.
11. Redmond EJ, O'Kelly T, Flood HD. The effect of bladder filling rate on the voiding behavior of patients with overactive bladder. *J Urol* 2019;**202**:326−32.
12. Jia J, Wu G, Zhang H, Wang F, Gu X, Dorma D, et al. Magnetic-driven hydrogel robots loaded with mitomycin for active therapy of bladder cancer. *ACS Appl Mater Interfaces* 2025;**17**:36366−76.
13. Lee JG, Petraccione J, Trese KA, Hughes AC, Ausec TR, Salzmann-Sullivan M, et al. Soft extrudable dendritic particles with nanostructured tendrils for local adhesion and drug release to bladder cancers. *Adv Mater* 2025;**37**:e2505231.
14. Chen Y, Cao X, Yao J, Hu Z, Luo Y, Li G, et al. Enhancing under-urine adhesion and bladder adaptation of silk fibroin hydrogels with tea polyphenols for hemorrhagic cystitis. *Int J Biol Macromol* 2024;**283**: 137487.
15. Yang Y, Yang GW, Lu JJ, Chen HR, Guo YQ, Yang N, et al. Fabrication of levofloxacin-loaded porcine acellular dermal matrix hydrogel and functional assessment in urinary tract infection. *J Nanobiotechnol* 2024;**22**:52.
16. Jhang JF, Lin TY, Ho HC, Jiang YH, Hsu YH, Birder LA, et al. Deficits of urothelial cell proliferation, cytoskeleton, and barrier function protein expressions in patients with recurrent and persistent urinary tract infections. *Low Urin Tract Symptoms* 2021;**13**:203−9.
17. Jiang YH, Jhang JF, Hsu YH, Ho HC, Lin TY, Birder LA, et al. Urothelial health after platelet-rich plasma injection in intractable recurrent urinary tract infection: improved cell proliferation, cytoskeleton, and barrier function protein expression. *Low Urin Tract Symptoms* 2021;**13**:271−8.
18. Nik-Ahd F, Lenore Ackerman A, Anger J. Recurrent urinary tract infections in females and the overlap with overactive bladder. *Curr Urol Rep* 2018;**19**:94.
19. Ke QS, Lee CL, Kuo HC. Recurrent urinary tract infection in women and overactive bladder — is there a relationship?. *Tzu Chi Med J* 2021;**33**:13−21.
20. Shan X, Littlejohn JE, Peng K, Ji F, Liu H. The effect of perioperative AKI on surgical outcomes. *Anesthesiol Perioper Sci* 2023;**1**:28.
21. Feeney C, Gorman G, Stefanetti R, McFarland R, Turnbull D, Harding C, et al. Lower urinary tract dysfunction in adult patients with mitochondrial disease. Neurourology and urodynamics. *Neurourol Urodyn* 2020;**39**:2253−63.
22. Chen L, Tang J, Zuo X, Li B, Liu C, Hong S, et al. SIRT1 alleviates oxidative stress-induced mitochondrial dysfunction and mitochondria-associated membrane dysregulation in stress urinary incontinence. *Cell Prolif* 2025;**58**:e70009.
23. Abo-Kamar AM, Mustafa AA, Al-Madboly LA. Purified $\alpha$-Amylase from *Bacillus cereus* exhibits antibiofilm and antiquorum sensing activities against uropathogenic *Escherichia coli*, downregulating fimH, and papC virulence genes: implications for urinary tract infections. *BMC Microbiol* 2024;**24**:502.
24. Guevara A, Armknecht K, Kudary C, Nallathamby P. PLGA nanoparticles formulations loaded with antibiotics induce sustained and controlled antibiotics release for prolonged antibacterial action against MRSA, and pseudomonas aeruginosa FRD1. *Mil Med* 2024;**189**: 230−8.
25. Al-Enizi AM, Ahamad T, Al-Hajji AB, Ahmed J, Chaudhary AA, Alshehri SM. Cellulose gum and copper nanoparticles based hydrogel as antimicrobial agents against urinary tract infection (UTI) pathogens. *Int J Biol Macromol* 2018;**109**:803−9.
26. Zhang S, Liang X, Gadd GM, Zhao Q. Superhydrophobic coatings for urinary catheters to delay bacterial biofilm formation and catheter-associated urinary tract infection. *ACS Appl Bio Mater* 2020;**3**: 282−91.
27. Shi FK, Zhong M, Zhang LQ, Liu XY, Xie XM. Robust and self-healable nanocomposite physical hydrogel facilitated by the synergy of ternary crosslinking points in a single network. *J Mater Chem B* 2016;**4**:6221−7.
28. Gao Y, Peng K, Mitragotri S. Covalently crosslinked hydrogels *via* step-growth reactions: crosslinking chemistries, polymers, and clinical impact. *Adv Mater* 2021;**33**:e2006362.
29. Wang L, Yang K, Li X, Zhang X, Zhang D, Wang LN, et al. A double-crosslinked self-healing antibacterial hydrogel with enhanced mechanical performance for wound treatment. *Acta Biomater* 2021;**124**: 139−52.
30. Liang Y, Li Z, Huang Y, Yu R, Guo B. Dual-dynamic-bond cross-linked antibacterial adhesive hydrogel sealants with on-demand

removability for post-wound-closure and infected wound healing. *ACS Nano* 2021;**15**:7078−93.
31. Hu L, Cheng S, Li Y, Geng S, Ma Y, Han X. Chitosan-Zn chelate downregulates TLR4-NF-$\kappa$B signal pathway of inflammatory response and cell death-associated proteins compared to inorganic zinc. *Biol Trace Elem Res* 2018;**184**:92−8.
32. Ke CL, Deng FS, Chuang CY, Lin CH. Antimicrobial actions and applications of chitosan. *Polymers* 2021;**13**:904.
33. Bourguignon LY. Matrix hyaluronan-activated CD44 signaling promotes keratinocyte activities and improves abnormal epidermal functions. *Am J Pathol* 2014;**184**:1912−9.
34. Murakami T, Otsuki S, Okamoto Y, Nakagawa K, Wakama H, Okuno N, et al. Hyaluronic acid promotes proliferation and migration of human meniscus cells *via* a CD44-dependent mechanism. *Connect Tissue Res* 2019;**60**:117−27.
35. Cirillo N. The hyaluronan/CD44 axis: a double-edged sword in cancer. *Int J Mol Sci* 2023;**24**:15812.
36. Mutlu N, Liverani L, Kurtuldu F, Galusek D, Boccaccini AR. Zinc improves antibacterial, anti-inflammatory and cell motility activity of chitosan for wound healing applications. *Int J Biol Macromol* 2022; **213**:845−57.
37. Trempe JF, Gehring K. Structural mechanisms of mitochondrial quality control mediated by PINK1 and Parkin. *J Mol Biol* 2023;**435**: 168090.
38. Narendra DP, Youle RJ. The role of PINK1-Parkin in mitochondrial quality control. *Nat Cell Biol* 2024;**26**:1639−51.
39. Bian X, Teng T, Zhao H, Qin J, Qiao Z, Sun Y, et al. Zinc prevents mitochondrial superoxide generation by inducing mitophagy in the setting of hypoxia/reoxygenation in cardiac cells. *Free Radic Res* 2018;**52**:80−91.
40. Chen GH, Song CC, Zhao T, Hogstrand C, Wei XL, Lv WH, et al. Mitochondria-dependent oxidative stress mediates ZnO Nanoparticle (ZnO NP)-induced mitophagy and lipotoxicity in freshwater teleost fish. *Environ Sci Technol* 2022;**56**:2407−20.
41. Alsailawi HA, Alasadi RT, Abbood SF, Mudhafar M, Mohammed RK, Al-ogaili AH, et al. Effect of zinc sulfate on biochemical parameters, histopathological, histochemical and immunological in male albino rats. *Multidiscip Sci* 2024;**6**:2024219.
42. Walter A, Krämer K, Most E, Pallauf J. Zinc availability from zinc lipoate and zinc sulfate in growing rats. *J Trace Elem Med Biol* 2002; **16**:169−74.
43. Johnson PE, Hunt JR, Ralston NV. The effect of past and current dietary Zn intake on Zn absorption and endogenous excretion in the rat. *J Nutr* 1988;**118**:1205−9.
44. Anchan M, Hande A, Deshpande S, Patel R, Kalthur G, Joshi JM, et al. C57BL/6J mice best recapitulate fibrosis and inflammatory pathophysiology in syngeneic mouse model of endometriosis. *Sci Rep* 2025;**15**:29024.
45. Zwaans BMM, Wegner KA, Bartolone SN, Vezina CM, Chancellor MB, Lamb LE. Radiation cystitis modeling: a comparative study of bladder fibrosis radio-sensitivity in C57BL/6, C3H, and BALB/c mice. *Phys Rep* 2020;**8**:e14377.